

¹ **MicroBooNE: Neutron Induced Cosmogenic π^0 's**

² **Ryan A.Grosso**

³ Submitted in partial fulfillment of the
⁴ requirements for the degree
⁵ of Doctor of Philosophy
⁶ in the Graduate School of Arts and Sciences

⁷ **UNIVERSITY OF CINCINNATI**

⁸ 2017

9

10

©2017

11

Ryan A.Grosso

12

All Rights Reserved

¹³ Table of Contents

¹⁴	List of Figures	iii
¹⁵	List of Tables	iv
¹⁶	1 Introduction	1
¹⁷	2 Neutrinos & Neutrino Oscillations	3
¹⁸	2.1 The History the Neutrino	3
¹⁹	2.2 Discovery of the Neutrino	5
²⁰	2.3 Neutrinos in the Standard Model	8
²¹	2.4 Neutrino Interactions	9
²²	2.5 Neutrino Mass and Flavor Oscillations	12
²³	2.6 Sterile Neutrinos	17
²⁴	3 The MicroBooNE Detector	18
²⁵	3.1 Brief History of LAR-TPC's	18
²⁶	3.2 Introduction	19
²⁷	3.3 Time Projection Chamber	20
²⁸	3.4 Light Collection	26
²⁹	3.5 Electronics Readout	28
³⁰	4 Booster Neutrino Beam	30
³¹	4.1 Primary Beam, Target and Horn	31
³²	4.2 Neutrino Flux Prediction	32

³³	5 Low Energy Excess and Relevant Cross Sections	35
³⁴	5.1 Overview	35
³⁵	5.2 LSND Excess	35
³⁶	5.3 Miniboone Excess	37
³⁷	5.4 Neutral Current π^0 production	38
³⁸	5.5 NC-Pi0 in Carbon vs Argon	40
³⁹	6 Cosmogenic π^0's at MicroBooNE	41
⁴⁰	6.1 Motivation	41
⁴¹	6.2 Traditional Reconstruction	43
⁴²	6.3 Wire Cell Imaging	44
⁴³	6.4 Pattern Recognition	45
⁴⁴	6.4.1 Clustering	46
⁴⁵	6.5 Track and Shower Selection	48
⁴⁶	6.5.1 Track Removal	48
⁴⁷	6.5.2 Single π^0 Reconstruction	48
⁴⁸	6.6 Single π^0 cosmic sample	52
⁴⁹	7 Results	56
⁵⁰	7.1 Reconstructed Variables	56
⁵¹	7.2 Monte Carlo Simulation	57
⁵²	7.3 Data	59
⁵³	8 Conclusions	60
⁵⁴	I Appendices	61

⁵⁵ List of Figures

56	2.1 Cowan and Reines first proposed neutrino experiment.	5
57	2.2 The Hadron production cross section around the Z^0 resonance from LEP.	7
58	2.3 The Standard Model	9
59	2.4 Charge and Neutral Current Interactions	12
60	2.5 This plot shows the appearance and disappearance curves for a 2-flavor ap-	
61	proximation as a function of baseline. The values of $\Delta m^2 = 0.0025\text{eV}^2$ and	
62	$\sin^2 \theta = 0.14$ are used.	14
63	2.6 Neutrino Mass Hierarchy	16
64	3.1 Diagram of a Time Projection Chamber	19
65	3.2 MicroBooNE TPC	21
66	3.3 MicroBooNE wires measured linear mass density	22
67	3.4 Tensioning system	23
68	3.5 Multiple wire planes installed in MicroBooNE	24
69	3.6 MicroBooNE tension measuring device	25
70	3.7 MicroBooNE tension map	26
71	3.8 MicroBooNE tension histogram	26
72	3.9 PMT optical unit	27
73	3.10 PMT optical unit	28
74	3.11 Detector Electronic layout	29
75	4.1 The Booster Neutrino Campus	30
76	4.2 BNB Target	32

77	4.3	Booster Neutrino Beamline	33
78	4.4	BNB Target	34
79	5.1	LSND Excess	36
80	5.2	MiniBooNE Event topology	38
81	5.3	MiniBooNE excess for ν and $\bar{\nu}$	39
82	5.4	pi0production	40
83	6.1	Icarus Cosmic π^0	43
84	6.2	Wire Cell reconstruction of CORSIKA MC viewed in the BEE viewer	46
85	6.3	Shower merging graphic	48
86	6.4	pi0Photon	49
87	6.5	Reconstructed energy sum and energy product for shower pairs. Both, the reconstructed energy sum and product is less than the true energy deposited.	50
89	6.6	pi0Photon	51
90	6.7	pi0Photon	52
91	6.8	pi0Photon	53
92	6.9	Cosmic π^0 production by parent process	54
93	6.10	pi0Photon	55
94	7.1	Enhanced Signal Sample	57
95	7.2	Background Sample	58

⁹⁶ List of Tables

⁹⁷	4.1 Beam Production Systematics	34
---------------	---	----

⁹⁸ Chapter 1

⁹⁹ Introduction

¹⁰⁰ This thesis describes work towards electromagnetic shower reconstruction and steps towards
¹⁰¹ a neutral current single π^0 cross section measurement motivated from reconstruction tech-
¹⁰² niques used for neutron induced cosmogenic π^0 analysis. This thesis will use data from
¹⁰³ the MicroBooNE Liquid Argon Time Projection Chamber(LArTPC) located at the Fermi
¹⁰⁴ National Accelerator in Batavia, Il.

¹⁰⁵

¹⁰⁶ To begin, Chapter 2 will provide some background about the neutrino. We will begin by
¹⁰⁷ presenting the initial premise for the need of a neutrino-like particle. Then, we will describe
¹⁰⁸ the theoretical framework used to address how they interact the standard model. Finally we
¹⁰⁹ will present the phenomenon known as neutrino oscillation and provide some mathematical
¹¹⁰ framework to describe it. Chapter 3 begins with a brief history of the LArTPC detector
¹¹¹ technology and its use as a high precision neutrino detector. The chapter continues to
¹¹² explain in depth the various subsystems that constitute the MicroBooNE detector. Chapter
¹¹³ 4 will describe how a neutrino beam is produced and delivered to the MicroBooNE detector.
¹¹⁴ It will focus on Fermilab's Booster Neutrino Beam(BNB) which generates a beam of nearly
¹¹⁵ pure ν_μ or $\bar{\nu}_\mu$ around 1GeV in average energy. Chapter 5 will present in detail the claims
¹¹⁶ of the electromagnetic ν_e -like excess first seen by the LSND experiment and then later
¹¹⁷ verified by the MiniBooNE experiment. This chapter will also discuss the neutral current
¹¹⁸ cross section, which is the main background in the MiniBooNE excess claim. Chapter
¹¹⁹ 6 will introduce MicroBooNE's cosmogenic background and motivate the importance of

understanding the cosmic rate. Here, we will also discuss the motivation to use cosmic π^0 events as a means of calibrating the detector energy scale. The cosmic backgrounds are addressed for the oscillation analysis and a future neutral current 1 π^0 measurement. Next, this chapter will address simulation, reconstruction, and event selection. Chapter 7 will present results from MicroBooNE cosmics data addressing the cosmic π^0 rate from neutral induced events.

¹²⁶ Chapter 2

¹²⁷ Neutrinos & Neutrino Oscillations

¹²⁸ 2.1 The History the Neutrino

¹²⁹ The story of the neutrino began in Paris on a cloudy winter day in the year 1896. Parisian
¹³⁰ native, Henri Becquerel was experimenting with uranium salts and investigating the newly
¹³¹ discovered x-ray radiation. [] He hypothesized that when the salts were energized by sun-
¹³² light they would produce the x-ray radiation. This hypothesis was disproven on the cloudy
¹³³ February 27th day when his experiment still detected radiation emitting from the salts in
¹³⁴ the absence of the sun. Becquerel had discovered radioactivity. In the coming years, this
¹³⁵ phenomena was supported by the work of Marie and Pierre Curie in studying the radioac-
¹³⁶ tivity of the element Thorium which lead to their discovery of the elements Polonium and
¹³⁷ Radium. These discoveries would later win Becquerel and the Currie's the 1903 Nobel Prize
¹³⁸ in Physics.

¹³⁹

¹⁴⁰ After radioactivity became an accepted phenomena in the science community, Ernst
¹⁴¹ Rutherford discovered that radioactive decay products came in two different forms. He
¹⁴² labeled them as α -decay and β -decay. At the time, beta decay was believed to be a two body
¹⁴³ decay where a nucleus A decays into a lighter nucleus A' and a β -particle(electron). The
¹⁴⁴ outgoing energy of the electron from a two body decay is given by equation 2.1. Assuming
¹⁴⁵ conservation of energy, the value of the outgoing energy should be a discrete.

$$E_e = \frac{m_A^2 + me^2 - m_{A'}^2}{2m_A} \quad (2.1)$$

146 In 1914, James Chadwick had discovered that the energy spectrum of the β -particles
 147 were continuations as opposed to mono-energetic. While some scientist were willing to
 148 abandon the requirement of energy conservation, others found this to be an unpalatable
 149 solution. Unable to attend the 1930 Tubingen physics conference in Germany, Wolfgang
 150 Pauli wrote a letter to the attendees in which he proposed the first idea of the neutrino.
 151 An excerpt from his famous December 4th letter is translated from German below [].

152 I have hit upon a desperate remedy to save the “exchange theorem” of statistics
 153 and the law of conservation of energy. Namely, the possibility that there could
 154 exist in the nuclei electrically neutral particles, that I wish to call neutrons,
 155 which have spin 1/2 and obey the exclusion principle and which further differ
 156 from light quanta in that they do not travel with the velocity of light. The
 157 mass of the neutrons should be of the same order of magnitude as the electron
 158 mass and in any event not larger than 0.01 proton masses. The continuous beta
 159 spectrum would then become understandable by the assumption that in beta
 160 decay a neutron is emitted in addition to the electron such that the sum of the
 161 energies of the neutron and the electron is constant...

162 In 1932, Chadwick discovered the neutron we know of today. Unfortunately, this neutron
 163 was too heavy to be the particle that Pauli had proposed. Expanding on Pauli’s work, Enrico
 164 Fermi proposed a more complete picture of beta decay and renamed Pauli’s ‘neutron’ to
 165 what is commonly called a *neutrino*. Fermi’s theory directly coupled the neutron with a
 166 final state proton, electron, and neutrino. This theory of beta decay, $n \rightarrow p + e^- + \bar{\nu}_e$
 167 preserves the law of conservation of energy and would later prove to be a more accurate
 168 descriptor of the process.

¹⁶⁹ **2.2 Discovery of the Neutrino**

¹⁷⁰ Measuring and detecting neutrinos is a tricky business. In the 1950's, Clyde Cowan and
¹⁷¹ Frederick Reines set out to directly measure neutrino interactions for the first time. If a free
¹⁷² neutrino existed, they hypothesized that they could detect the byproducts from the inverse
¹⁷³ beta decay $\bar{\nu}_e + p \rightarrow e^+ + n$. They realized that such a measurement would require a very
¹⁷⁴ intense neutrino source and a large detector. Their first proposal, which was approved, was
¹⁷⁵ to detonate a nuclear bomb to supply the large, instantaneous source of neutrinos. A large
¹⁷⁶ detector filled with liquid scintillator would free fall down a mind shaft recording flashes
¹⁷⁷ of light from the ionizing positrons before landing on a bed of feathers and foam rubber.
¹⁷⁸ The original experimental schematic is shown in Figure 2.1. At that time, the theorized
¹⁷⁹ neutrino cross section was $10^{-43} \text{ cm}^2/\text{proton}$ while the existing measured limit was still 7
¹⁸⁰ orders of magnitude short in sensitivity. The bomb experiment would have worked but
¹⁸¹ could not provide the level of sensitivity required to confirm detection for neutrino cross
¹⁸² sections below $10^{-39} \text{ cm}^2/\text{proton}$. This was due to background interactions that came in
¹⁸³ time directly from the bomb.

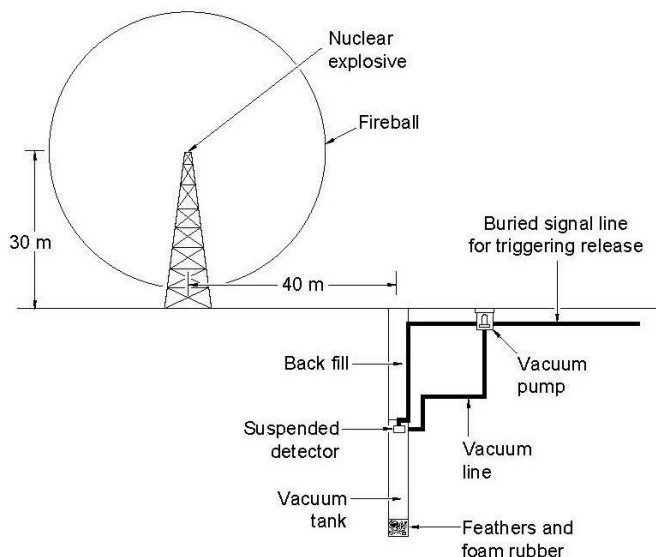
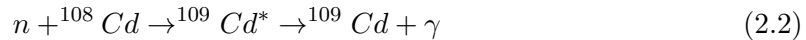


Figure 2.1: Original sketch of Cowan and Reines first proposed neutrino experiment.

Later, Reines realized tagging both the positron and neutron through a double coincidence would drastically reduce the backgrounds. This meant they could use a less intense neutrino source such as a nuclear reactor. They chose the Savannah River Plant near Augusta, Georgia which was estimated to produce neutrino fluxes on the order of $10^{12} - 10^{13}$ neutrinos/s/cm². The detector was composed of a water target that was doped with CdCl₂. As stated prior, the signal would rely on a double coincidence flash measured from photomultipiler tubes inside their detector. First, they would detect the positron as it annihilates with an electron via pair production ($e^+ + e^- \rightarrow \gamma + \gamma$). This is identified by two, back-to-back, coincident 0.511 MeV photons. Then, approximately 5μS later, a secondary photon would be detected which was produced from the neutron capture on Cadmium as shown in equation 2.2.



In 1956, only 25 years after Pauli's initial proposal of the neutrino, Cowan and Reines succeeded and provided the first direct experimental evidence of the electron flavor neutrino. In the subsequent years, the existence of two other flavors of neutrinos have been verified. In 1962, Lederman, Schwartz, and Steinberger discovered the ν_μ at Brookhaven Nation Laboratory by measuring neutrinos coming from pion decay. The ν_μ would be distinctly different from that of ν_e if the process $\nu_\mu + n \rightarrow p + e^-$ was forbidden. The results showed that the neutrinos from pion decay were indeed muon-like. Finally in 2000, the DONUT(Direct Observation of NeUtrino Tau) experiment stationed at Fermilab, made the first observed measurement of the ν_τ .

In 1956, C.S. Wu had shown that outgoing electron from beta decay maintained an opposing spin with respect to the spin of the parent nucleus. This turned out to be the first proof of maximal parity violation in weak interactions. Shortly thereafter, the neutrino helicity was first measured at Brookhaven National Labs by Maurice Goldhaber. In nature, neutrinos only have left handed helicity, while anti-neutrinos have right handed helicity. Helicity is frame dependent for particles with mass, which means there can be a reference frame in which the momentum vector can switch but the spin vector will not. For a

211 mass zero particles, this is not possible because the particle would already be traveling at
 212 the speed of light. This assumption is what lead to the believe that neutrinos were massless.

213 The number of active light neutrinos are well constrained by studying the decay of the
 214 Z^0 boson at LEP(Large Electron-Positron collider). LEP was an electron-positron collider
 215 ring with a circumference of approximately 27 km that supported four primary experiments
 216 (L3, ALEPH, OPAL and DELPHI). The facility was coined the phrase “Z-Factory” due
 217 to it’s ability to record approximately 1000 Z^0 boson decays every hour during optimal
 218 running conditions. The number of active neutrinos, N_ν is related to the width of the Z^0
 219 resonance. Using 17 million Z^0 decays, LEP was able to show that $N_\nu = 2.9840 \pm 0.0082$

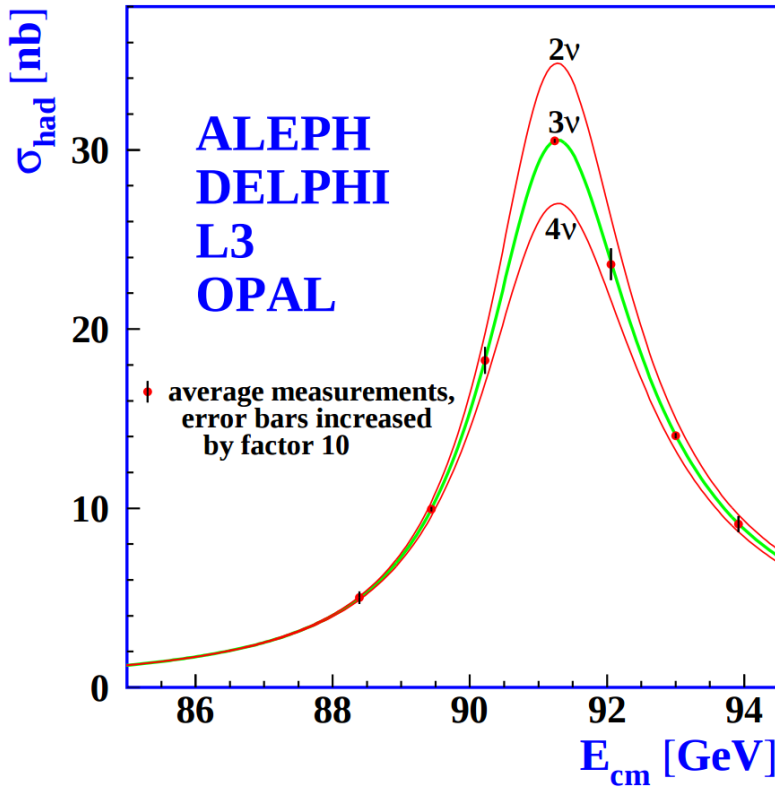


Figure 2.2: The Hadron production cross section around the Z^0 resonance from LEP. The curves for two, three, and four neutrino flavors are shown. The fit shows very compelling evidence of three active flavors of neutrinos.

220 2.3 Neutrinos in the Standard Model

221 In the later half of the 20th century, scientists were looking for a way to describe all the
222 fundamental forces and classify the known particles. The standard model of particle physics
223 is a phenomenological framework that describes the interaction of fundamental particles be-
224 tween the strong and electroweak forces. Having stood the test of time, the standard model
225 accurately predicts most elementary particle interactions, but, does have it's limitations.
226 The standard model does not account for gravity nor does it account for many new physics
227 issues such as dark matter or dark energy. Most importantly, as we will see in section 2.5,
228 it does not provide an accurate description of the neutrino.

229 The standard model consists of two types of particles, bosons and fermions. The funda-
230 mental bosons consist of two families: gauge bosons, which are typically the force carriers,
231 and scalar bosons, which refer to spin zero particles or fields. The gluon, photon, and the
232 weak boson are gauge bosons that mediate the strong, electromagnetic, and weak forces,
233 respectively. The Higgs boson is a scalar boson that possesses a nonzero vacuum expec-
234 tation value of 246GeV . This provides a mechanism for certain particles to gain mass
235 even though their symmetries would suggest zero mass. The fundamental fermions are also
236 divided into two families, quarks and leptons each having three generations. The quarks
237 compose two main categories of particles, baryons and mesons. Baryons consist of an en-
238 semble of 3 quarks. The most common and stable baryons in the universe are protons(uud)
239 and neutrons(udd). Meson consist of an ensemble of quark anti-quark pairs and tend to
240 have shorter lifetimes than their corresponding baryons. The lightest and most common
241 mesons are pions($u\bar{d}, d\bar{u}, u\bar{u}/d\bar{d}$) and kaons($u\bar{s}, s\bar{u}, d\bar{s}/s\bar{d}$). The leptons are also divided into
242 two families with three generations each. The charged leptons, most notably the electron,
243 interact via the strong and weak nuclear force and combine to form common baryonic mat-
244 ter. The neutral leptons are the neutrinos and only interact via the weak nuclear force.
245 More details such as, mass, charge, and spin for various particles are shown in figure 2.3

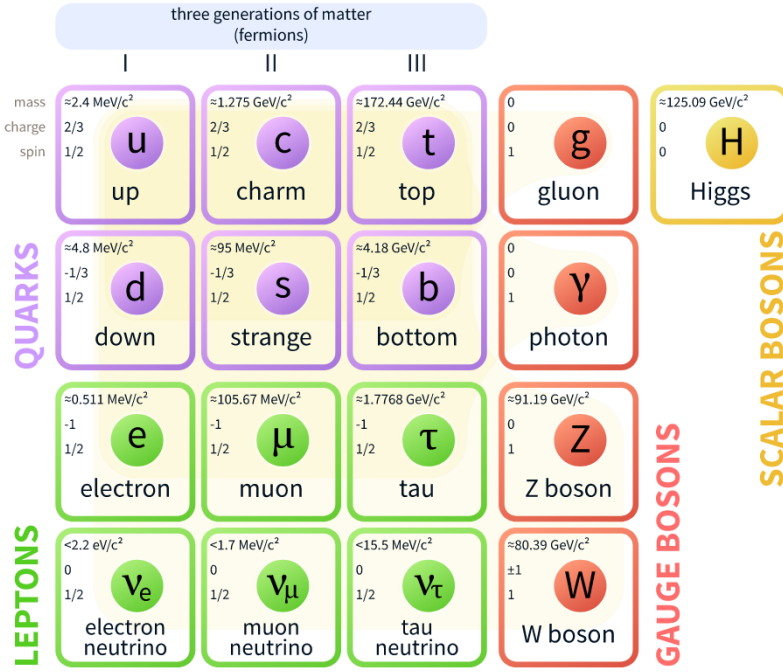


Figure 2.3: The current view of the standard model.

246 2.4 Neutrino Interactions

247 Neutrinos interact via the weak force. In the standard model, the weak force is unified
 248 with the electromagnetic force through an $SU(2) \otimes U(1)$ symmetry. The structure of the
 249 $SU(2)$ group symmetry accounts for the chirality of the fermion fields, along with ability to
 250 produce massive gauge bosons. The $U(1)$ group symmetry accounts for the massless photon
 251 propagator needed for electromagnetic interactions. For the quark and fermion families we
 252 define fermion fields in equations 2.3 and 2.4 , respectively. For formality we will define
 253 right(left)- handed neutrino(anti-neutrino) fields knowing that they will become irrelevant
 254 as the theory evolves:

$$\psi_1(x) = \begin{pmatrix} q \\ q' \end{pmatrix}_L , \quad \psi_2 = q_R , \quad \psi_3 = q'_R \quad (2.3)$$

$$\psi_1(x) = \begin{pmatrix} \nu \\ l \end{pmatrix}_L , \quad \psi_2 = \nu_R , \quad \psi_3 = l_R \quad (2.4)$$

255 We begin with the free Lagrangian, defined in equation 2.5, as it is already invariant in
 256 flavor space.

$$\mathcal{L}_{\text{free}} \equiv \bar{\psi}(i\cancel{\partial} - m)\psi = i\bar{\psi}(x)\gamma^\mu\partial_\mu\psi(x) - m\bar{\psi}(x)\psi(x) \quad (2.5)$$

257 To make the Lagrangian invariant under local $SU(2) \otimes U(1)$, the fermion derivatives
 258 have to be changed to covariant objects. This produces 4 different gauge parameters, shown
 259 in equations 2.6, which correspond to the 4 different gauge fields required to describe the
 260 W^\pm , Z^0 , and γ .

$$\begin{aligned} D_\mu\psi_1(x) &\equiv [\partial_\mu - ig\widetilde{W}_\mu(x) - ig'y_1B_\mu(x)]\psi_1(x) \\ D_\mu\psi_2(x) &\equiv [\partial_\mu - ig'y_2B_\mu(x)]\psi_2(x) \\ D_\mu\psi_3(x) &\equiv [\partial_\mu - ig'y_3B_\mu(x)]\psi_3(x) \end{aligned} \quad (2.6)$$

261 Where, σ^i are the Pauli spin matrices and B_μ represents a field imposed by an external
 262 source. We find that,

$$\begin{aligned} \widetilde{W}_\mu(x) &\equiv \frac{\sigma_i}{2} \left\{ \partial_\mu W_\nu^i - \partial_\nu^i + g\epsilon^{ijk}W_\mu^jW_\nu^k \right\} \\ B_{\mu\nu} &\equiv \partial_\mu B_\nu - \partial_\nu B_\mu \end{aligned} \quad (2.7)$$

263 The Lagrangian now satisfies $SU(2) \otimes U(1)$ symmetry between all gauge fields as shown
 264 in equation 2.8. It should be noted that the fermion fields and gauge bosons are required to
 265 be massless. This does not accurately describe the true interaction since 3 of the 4 gauge
 266 bosons are known to have mass, but the theory does allow an interface between neutrino
 267 interactions in the standard model.

$$\mathcal{L} = \sum_{j=0}^3 i\bar{\psi}_j(x)\gamma^\mu D_\mu\psi_j(x) \quad (2.8)$$

268 From equation 2.8, the terms that account for interaction of gauge bosons with the
 269 fermion fields are shown below in equation 2.9

$$\mathcal{L} \rightarrow g\bar{\psi}_1(x)\gamma^\mu\widetilde{W}_\mu\psi_1(x) + g'B_\mu\sum_{j=0}^3 y_j\bar{\psi}_j(x)\gamma^\mu\psi_j(x) \quad (2.9)$$

270 From this, we are then able to construct the Lagrangian for both the charged and neutral
 271 currents. The charge current Lagrangian is shown in equation 2.10.

$$\mathcal{L}_{CC} = \frac{g}{2\sqrt{2}} \left\{ W_\mu^\dagger [\bar{q}\gamma^\mu(1-\gamma_5)q' + \bar{\nu}\gamma^\mu(1-\gamma_5)\bar{l}] + \dots \right\} \quad (2.10)$$

272 The neutral current term in the Lagrangian contains gauge fields for both the Z boson
 273 and photon, which can be broken into two terms to account for a non-zero Z boson mass
 274 while leaving the photon massless through spontaneous symmetry breaking(SSB). This is
 275 done through an arbitrary rotation, as shown in equation 2.11, where θ_w is known as the
 276 Weinberg or weak mixing angle. This angle is important because it is the angle used to
 277 rotate through SSB giving the Z boson its mass.

$$\begin{pmatrix} W_\mu^3 \\ B_\mu \end{pmatrix} = \begin{pmatrix} \cos \theta_w & \sin \theta_w \\ -\sin \theta_w & \cos \theta_w \end{pmatrix} \times \begin{pmatrix} Z_\mu \\ A_\mu \end{pmatrix} \quad (2.11)$$

278 It is then possible to write the neutral current Lagrangian that accounts for the inter-
 279 action of the Z boson as shown in equation 2.13.

$$\mathcal{L}_{NC} = \frac{e}{2\sin(\theta_w)\cos(\theta_w)} Z_\mu \sum_f \bar{f}\gamma^\mu(v_f - \alpha_f\gamma_5)f \quad (2.12)$$

280 where,

$$g\sin(\theta_w) = g'\cos(\theta_w) = e \quad \text{and} \quad \cos(\theta_w) = \frac{M_w}{M_z} \quad (2.13)$$

281 The neutral current coupling constants, v_f & α_f , differ with respect to the various quark,
 282 charged and neutral lepton fields. The neutrinos can be described as interactions via the
 283 charged and neutral currents. The Feynman diagrams, shown in figure 2.4, depict how the
 284 leptons couple to the quarks via the current mediator.

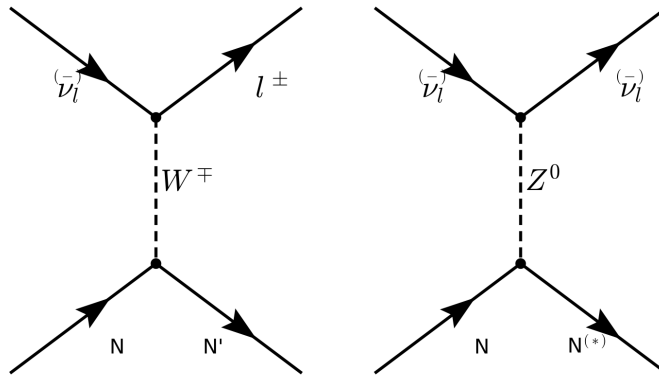


Figure 2.4: The Feynman diagram on the left describes a charged current(CC) neutrino interaction which transforms neutrinos into their corresponding charged leptons. In the CC interaction diagram the $N \rightarrow N'$ represents a changed nucleon charge. The diagram on the right shows the neutral current(NC) neutrino interaction with preserves the neutrino while it interacts. In the NC intearction diagram the $N \rightarrow N^*$ represents a same charge nucleon that could be at a higher resonance state.

2.5 Neutrino Mass and Flavor Oscillations

Neutrino oscillation is a quantum mechanical phenomenon in which the fraction of neutrino flavor changes while it propagates. This phenomena was first proposed in 1957 by Bruno Pontecorvo and relates the neutrino mass eigenstates with the flavor eigenstates through a rotation. This phenomena is best shown through a two neutrino flavor example, then extended into 3 flavors.

The mixing matrix for a two flavor neutrino case is:

$$\begin{pmatrix} \nu_e \\ \nu_\mu \end{pmatrix} = \begin{pmatrix} \cos \theta & \sin \theta \\ -\sin \theta & \cos \theta \end{pmatrix} \begin{pmatrix} \nu_1 \\ \nu_2 \end{pmatrix} \quad (2.14)$$

In this example, the flavor states are represented as ν_e and ν_μ which are expressed as a mixture of mass states ν_1 and ν_2 . For ascetic reasons, we chose ν_μ to be part of the example because most man made neutrino beams produce a relative pure sample of ν_μ . The framework for this example is commonly used as an oscillation approximation and can be generalized to satisfy any case of two distinctly different flavor neutrinos.

297 Using the two flavor formalism a pure ν_μ neutrino state can be expressed as equation
 298 2.15

$$|\nu_\mu(0)\rangle = -\sin \theta |\nu_1(0)\rangle + \cos \theta |\nu_2(0)\rangle \quad (2.15)$$

299 The evolution of the state is governed by solving the time dependent Schroedinger
 300 equation for the initial muon state:

$$|\nu_\mu(t)\rangle = e^{-i\frac{Et}{\hbar}} |\psi(0)\rangle = -e^{-i\frac{E_1 t}{\hbar}} \sin \theta |\nu_1\rangle + e^{-i\frac{E_2 t}{\hbar}} \cos \theta |\nu_2\rangle \quad (2.16)$$

301 Assuming neutrinos travel near the speed of light, we rewrite equation 2.16 using the
 302 relativistic approximation, along with setting $c = \hbar = 1$ and $p_1 = p_2 = p$:

$$|\nu_\mu(t)\rangle \simeq -e^{-i(p_1 + \frac{m_1^2}{2p_1})t} \sin \theta |\nu_1\rangle + e^{-i(p_2 + \frac{m_2^2}{2p_2})t} \cos \theta |\nu_2\rangle \quad (2.17)$$

303 with,

$$E = \sqrt{p^2 + m^2} = p \sqrt{1 + \frac{m^2}{p^2}} \approx p + \frac{m^2}{2p} \quad (2.18)$$

304 Next, the mass terms are grouped together and defined as the absolute square difference,
 305 $\Delta m^2 \equiv |m_2^2 - m_1^2|$. We find that if the mass are different then the mass eigenstates propagate
 306 at different frequencies and give rise the oscillatory behavior. The time dependent state can
 307 now be wrote as:

$$|\nu_\mu(t)\rangle = e^{-i\phi} (-\sin \theta |\nu_1\rangle + e^{+i\frac{\Delta m^2}{2p}t} \cos \theta |\nu_2\rangle) \quad (2.19)$$

with, $e^{-i\phi} \equiv e^{-i\left(p + \frac{m_1}{2p}\right)t}$

308 To calculate the probability of the initial ν_μ state being measured as a ν_e state at some
 309 later time t , we need to calculate the absolute value squared of the overlap between the
 310 states. Utilizing the relationship $\langle \psi_i | \psi_j \rangle = \delta_{i,j}$, the overlap between the states is:

$$\langle \nu_e | \nu_\mu(t) \rangle = e^{-i\phi} (-\sin \theta \cos \theta + \sin \theta \cos \theta e^{i\frac{\Delta m^2}{2p}t}) \quad (2.20)$$

³¹¹ The probability reduces to:

$$\begin{aligned}
 P(\nu_\mu \rightarrow \nu_e) &= |\langle \nu_e | \nu_\mu(t) \rangle|^2 \\
 &= e^{i\phi} e^{-i\phi} \sin^2 \theta \cos^2 \theta (-1 + e^{-i\frac{\Delta m^2}{p}t})(-1 + e^{+i\frac{\Delta m^2}{p}t}) \\
 &= \frac{1}{2} \sin^2 2\theta \left(1 - \cos \left(\frac{\Delta m^2}{2p} t \right) \right)
 \end{aligned} \tag{2.21}$$

³¹² Finally, from relativistic assumptions, we set $p = E_\nu$ as the outgoing neutrino energy
³¹³ and $t = L$ corresponds to the distance traveled.

$$P(\nu_\mu \rightarrow \nu_e) = \sin^2 2\theta \sin^2 \left(\frac{\Delta m^2 L}{4E_\nu} \right) \tag{2.22}$$

³¹⁴ From a proper accounting of numerical values of c and \hbar , equation 2.26 is more com-
³¹⁵ monly written as:

$$P(\nu_\mu \rightarrow \nu_e) = \sin^2 2\theta \sin^2 \left(1.27 \frac{\Delta m^2 L}{E_\nu} \right) \tag{2.23}$$

³¹⁶ This oscillation behavior is best visualized as a plot of the probability of appearance
³¹⁷ and disappearance as shown Figure 2.5.

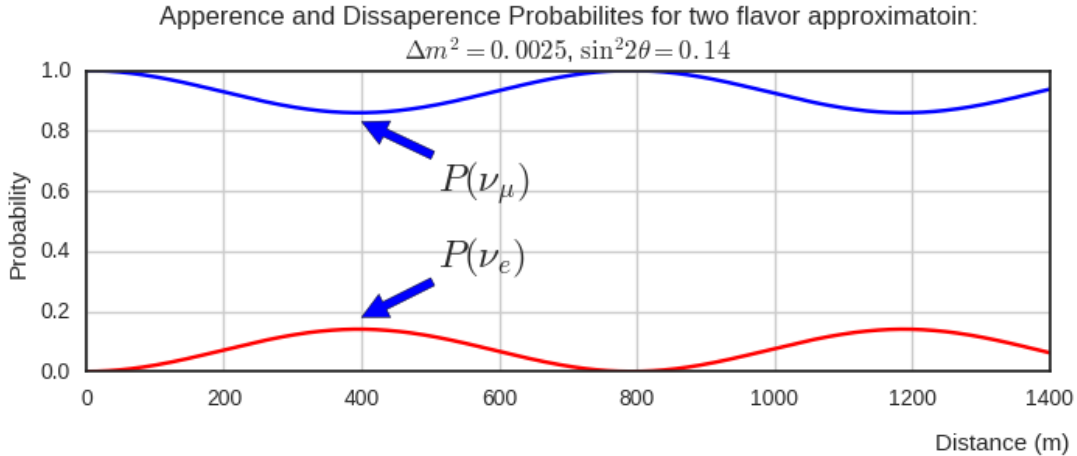


Figure 2.5: This plot shows the appearance and disappearance curves for a 2-flavor approximation as a function of baseline. The values of $\Delta m^2 = 0.0025 \text{ eV}^2$ and $\sin^2 \theta = 0.14$ are used.

As shown prior from figure 2.2, there are very good constraints on the number of active neutrinos. Extending this formalism to a 3 flavor case was done by Pontecorvo-Maki-Nakagawa-Sakata (PMNS). The PMNS matrix is a 3 dimensional unitary matrix which is parameterized by three mixing angles $\theta_{12}, \theta_{23}, \theta_{13}$ a complex phase δ . The three angle correspond to the mixing effect, while δ is known as the charge parity(CP) phase. If the CP-phase is non-zero, then neutrinos violate charge parity conservation which leads to the conclusion that neutrinos and anti-neutrinos interact differently with matter. The value for δ has yet to be observed.

$$U_{PMNS} = \begin{pmatrix} 1 & 0 & 0 \\ 0 & c(\theta_{23}) & s(\theta_{23}) \\ 0 & -s(\theta_{23}) & c(\theta_{23}) \end{pmatrix} \begin{pmatrix} c(\theta_{13}) & 0 & s(\theta_{13})e^{-i\delta} \\ 0 & 1 & 0 \\ -s(\theta_{13})e^{i\delta} & 0 & c(\theta_{13}) \end{pmatrix} \begin{pmatrix} c(\theta_{12}) & s(\theta_{12}) & 0 \\ -s(\theta_{12}) & c(\theta_{12}) & 0 \\ 0 & 0 & 1 \end{pmatrix} \quad (2.24)$$

where $c(\theta_{ij}) \equiv \cos \theta_{ij}$ and $s(\theta_{ij}) \equiv \sin \theta_{ij}$. The matrix equation is now put into a more compact manor that relates the mixing of the 3 neutrino generations.

$$\begin{pmatrix} \nu_e \\ \nu_\mu \\ \nu_\tau \end{pmatrix} = \begin{pmatrix} U_{e,1} & U_{e,2} & U_{e,3} \\ U_{\mu,1} & U_{\mu,2} & U_{\mu,3} \\ U_{\tau,1} & U_{\tau,2} & U_{\tau,3} \end{pmatrix} \begin{pmatrix} \nu_1 \\ \nu_2 \\ \nu_3 \end{pmatrix} \quad (2.25)$$

In it's most general form, the oscillation probability is:

$$P(\nu_\alpha \rightarrow \nu_\beta) = \delta_{\alpha,\beta} - 4 \sum_{j>i} U_{\alpha,i} U_{\beta,i} U_{\alpha,j}^* U_{\beta,j}^* \sin^2 \left(1.27 \frac{\Delta m_{ij}^2 L}{E_\nu} \right) \quad (2.26)$$

From equation 2.26, we see that the oscillation probability is depended on the mass difference between states. There is currently no method to directly measure the mass of any given neutrino. Therefore, there is an allowed ambiguity in the mass ordering of all three neutrino states. This is called the neutrino hierarchy problem. However, we do know that the difference between m_1 and m_2 is small relative to m_3 . Using this, we can build a picture of the fraction of different flavor eigenstates corresponding to their various mass states for both types of hierarchy.

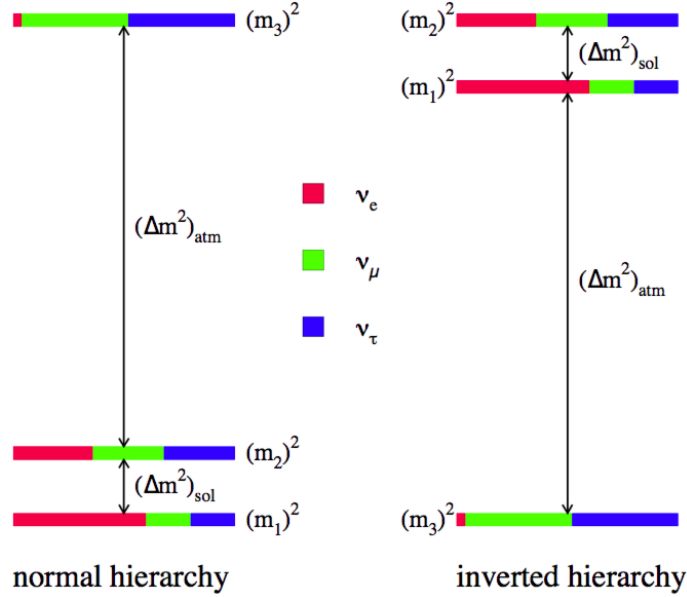


Figure 2.6: The two possible ordering for the 3 active neutrino mass eigenstates.

336 Many experiments have measures various elements of the PMNS matrix with neutrinos
 337 coming from accelerators, reactors, and solar sources. Currently, normal hierarchy
 338 ($m_1 < m_2 < m_3$) is favored, therefore we will show (table 2.27) the current Particle Data
 339 Group(PDG)[] best fit values for oscillation parameters with respect to normal hierarchy.

$$\begin{aligned}
 \Delta m_{21}^2 &= 7.37 \times 10^{-5} eV^2 \\
 \Delta m_{32}^2 &= 2.50 \times 10^{-3} eV^2 \\
 \sin(\theta_{12}) &= 0.297 \\
 \sin(\theta_{23}) &= 0.437 \\
 \sin(\theta_{13}) &= 0.0214 \\
 \delta/4 &= 1.35
 \end{aligned} \tag{2.27}$$

³⁴⁰ **2.6 Sterile Neutrinos**

³⁴¹ It is well accepted, from measurements at LEP[], that there are only 3 neutrinos that couple
³⁴² through the weak interaction. Mathematically, nothing prohibits a theory that allows for
³⁴³ neutrino mixing with other neutrino states beyond the 3 active states. These states, since
³⁴⁴ they do not interact weakly, are called 'sterile neutrinos'. Extending the 3 flavor oscillation
³⁴⁵ model to include any number of sterile neutrinos may be a possibility to address some the
³⁴⁶ currently unexplained results in the neutrino physics fields. Each additional state requires
³⁴⁷ an extra dimension to be added to the PMNS matrix. The sterile eigenstates are then
³⁴⁸ defined as

$$|\nu_{s_i}\rangle = \sum_j^{3+N} U_{s_i,j} |\nu_j\rangle \quad (2.28)$$

³⁴⁹ where N is the number of sterile neutrinos. The necessity for additional sterile neutrinos
³⁵⁰ was prompted by the LSND experiment and later supported by the MiniBooNE. experiment.
³⁵¹ Both experiments are explained in depth in chapter 5. Each experiment found an excess
³⁵² of electron-like events at low energy. This suggested a Δm^2 parameter space observed to
³⁵³ be 1eV^2 larger than expected and strongly contradicted the results of many other results
³⁵⁴ which had Δm^2 around $\mathcal{O}(10^{-3}\text{eV}^2)$ and $\mathcal{O}(10^{-5}\text{eV}^2)$. This precipitated the need for
³⁵⁵ further exploration of the LSND and MiniBooNE claims with more sophisticated detector
³⁵⁶ technologies. The MicroBooNE experiment was proposed in 2007¹ and will be the focal
³⁵⁷ point for this thesis.

358 Chapter 3

359 The MicroBooNE Detector

360 3.1 Brief History of LAr-TPC's

361 The surprising nature of neutrinos quickly prompted the need for precision measurements
362 of their interactions. Unfortunately, the low neutrino cross section posed a hurdle to build
363 a high statistics detector. In 1977, C.Rubbia propose a Liquid Argon Time Projection
364 Chamber (LArTPC) as large, high precision neutrino detector.^[1] In 2001, The ICARUS col-
365 laboration commissioned the T600 detector which was one of the first large scale LArTPC's
366 to be used as a neutrino detector. ^[2] The T600, which is comprised 760 tons of liquid argon
367 and commissioned in Pavia, Italy using cosmic rays as a proof of principle. Later the T600
368 was place underground in Hall B of Laboratori Nazionali del Gran Sasso (LNGS) which is
369 located 730 km from the source of the CERN neutrino beam.

370 In 2009, the AgroNeut collaboration, commissioned a small LArTPC in a 175 liter
371 vacuum jacketed cryostat. The ArgoNeut TPC was comprised of 3 wire planes and operated
372 at a drift field of 500 V/cm. The detector was placed just in front of the MINOS near
373 detector in the NuMI beam at Fermi National Accelerator Laboratory(FNAL)^[3]. AgroNeut
374 collected thousands of neutrino and antineutrino events providing valuable physics data and
375 detector R&D for future experiments with LArTPC's.

376 The MicroBooNE (the Micro Booster Neutrino Experiment) detector, which will be
377 discussed in depth throughout this chapter, is the first multi-ton LArTPC to be fully op-
378 erational in the U.S. The MircoBooNE detector design pioneered many new detector R&D

379 concepts such as: the ability to maintain high LAr purity in an unevaluated vessel, imple-
 380 mentation of low noise electronic readouts at liquid cryogenic temperatures and advances
 381 in reconstruction techniques. MicroBooNE also, supports a robust, high statistics physics
 382 program to address the MiniBooNE Low Energy Excess and various cross section measure-
 383 ments. MicroBooNE was commissioned and began taking cosmic ray data in the summer of
 384 2015. In October 2015 it began taking neutrino data. Shortly there after, the first neutrino
 385 event candidates were identified. []

386 3.2 Introduction

387 The MicroBooNE detector utilizes 170 tons of liquid argon to sustain 87 tons of active
 388 detector mass. It is located at the Liquid Argon Test Facility (LARTF) which is 470
 389 m downstream of the Booster Neutrino Beam-line(BNB) source at the Fermilab National
 390 Accelerator Lab (FNAL) in Batavia, Illinois. The detector is the first large scale LArTPC
 391 to be deployed, commissioned and fully operated in the US.

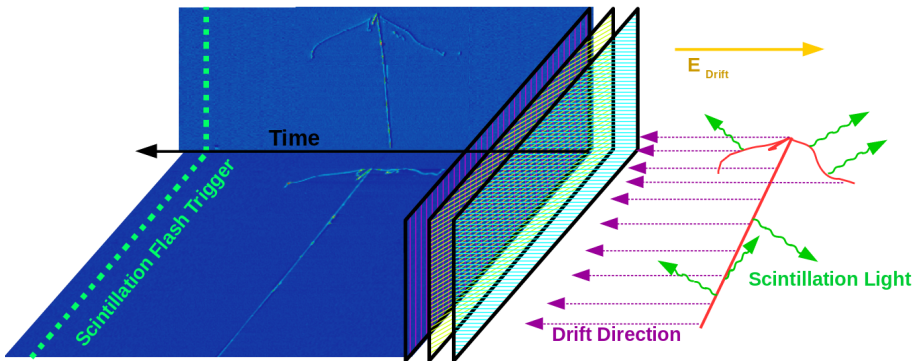


Figure 3.1: This diagram explains how a TPC works. First, charged tracks ionize the argon. The remaining ions produce prompt scintillation light and the corresponding electrons begin to drift towards the wires due to the presence of the electric field. When the drift electrons reach the wire planes a 2D image is produced for each plane. When combining the 2D images from multiple planes along with the scintillation light information a 3D reconstruction is possible.

392 The general principle of a LArTPC involves utilizing two properties of LAr, scintillation

393 light and ionization. Charged particles travel through the argon and produce scintillation
394 light which is collected by photomultiplier tubes (PMT's). A uniform electric field is applied
395 over active volume which transports the ionization electrons to a series of wire planes.
396 Assuming the argon is pure and has minimal electro-negative contaminants, the wire planes
397 then measure the induced or collected charge signal from the drifting electrons. The planes
398 are each oriented at a different pitch angles. Each plane then can then produce a two
399 dimensional image of the event as a function of wire and time. Combining multiple planes
400 along with the PMT information allows for the object to be fully reconstructed in three
401 dimensions. A diagram of the TPC concept is show in Figure 3.1. In the following sections
402 the TPC, light collection system, and electronics are described in detail.

403 **3.3 Time Projection Chamber**

404 The TPC is the core of the MicroBooNE detector and forms a rectangular prism with
405 dimensions $2.3m \times 2.6m \times 10.4m$ which contains 87t of LAr. The longest dimension, which
406 in MicroBooNE's coordinate system is refereed to as the z-direction, is oriented on axis
407 of the BNB. The majority of the TPC materials are composed of 304V stainless steel
408 and G10. Stainless steel was chosen due to it's low magnetic susceptibility, resistance to
409 corrosion/oxidation, and ability to maintain it's strength in cryogenic temperatures. G10
410 was chosen due to it's ability to perform well as an insulator in cryogenic environments.



Figure 3.2: The MicroBooNE TPC is shown here. On the far right is the flat cathode plane. The far left shows the 8,456 anode wires installed. The field cage tubes, which provide the uniform electric field, span the length between the anode and cathode.

411 The TPC field cage, which provides the uniform electric field through the detector
 412 volume, and was designed to produce field strengths up to 500 v/cm in liquid argon. The
 413 field cage consists of a total of 64 stainless steel rectangular loops that are supported and
 414 evenly spaced by a G10 holder. The cathode plane is a series flat stainless steel sheets that
 415 is opposite the anode sense wires. Figure 3.2 shows the MicroBooNE TPC.

416 Every piece that was used in the MicroBooNE detector was thoroughly cleaned. Many
 417 pieces were cleaned in an ultrasonic cleansing bath while others were cleaned by hand.
 418 The detector was constructed in a clean environment that maintained positive pressure to
 419 mitigate the accumulation of dust. A complete description of the process is summarize in
 420 a separate technical note. []

421 MicroBooNE has a total of 8,265 sense wires that form 3 unique wire planes, one vertical
 422 collection plane (Y) and two induction planes (U,V) oriented at ± 60 relative the Y plane.
 423 The wire planes are separated by 3 mm. The wires in each plane are evenly spaced by 3
 424 mm pitch on carrier boards. The Y plane consists of 3,456 wires with a total of 108 carrier
 425 boards that accommodate 32 wires each. Each of the U and V planes consist of 2,400 wires
 426 with a total of 150 carrier boards that accommodate 16 wires each. The wires themselves
 427 are made of 304V stainless steel and are $150 \pm 5\mu\text{m}$ in diameter. A $2\mu\text{m}$ layer of copper
 428 is plated over the wires to decrease the resistivity from $40\Omega/\text{m}$ to $3\Omega/\text{m}$. The reduced

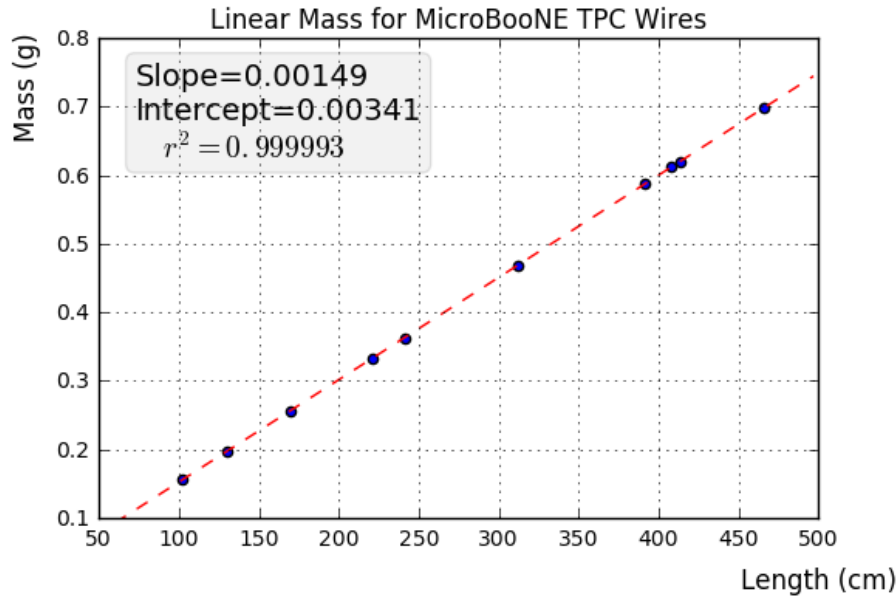


Figure 3.3: This plot is for a small sample used to cross check the linear mass density measured from the wire dealer. The slope from this plot represents the linear mass density and was found to be consistent with the value 0.149g/m

429 resistivity aids in noise reduction at cryogen temperatures. Finally the wire is covered in
 430 and outer layer 0.1 μ m of gold to prevent the copper from oxidizing over time. The linear
 431 mass density of a small sample of wires was measured and is shown in figure 3.3.

432 The wires were designed to installed at a nominal tension of 6.97 N. To account for this,
 433 the carrier boards were installed onto a series of tensioning bars on the anode frame. These
 434 tensioning system, as shown in figure 3.4, allowed for fine tune adjustments to be made to
 435 separate sections of wires.

436 There are a total of 12 tensioning bars, 2 sets of 5 that traverse the entire top and bottom
 437 length of the anode frame, and 2 spanning the entire height of the upstream and downstream
 438 sections of the anode frame. Bronze jacking screws were used for final adjustments once
 439 all the wires were installed. Bronze was chosen since it has a similar thermal expansion
 440 coefficient to stainless steel and it is a softer metal which helps mitigate the risk of cold
 441 welding with stainless steel during the tensioning process.

442 In preparation for installing the actual detector wires, an installation team was trained

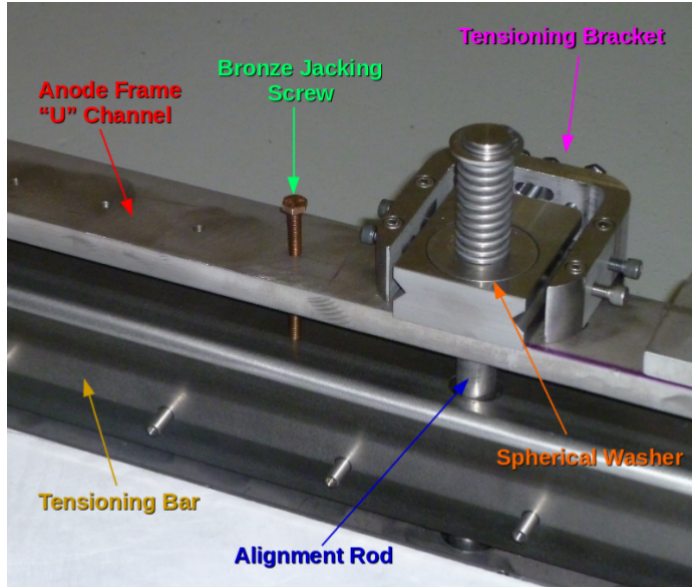


Figure 3.4: The MicroBooNE tension system. Wire carrier boards (not shown here) are mounted on the tensioning bar. The tensioning bar is able to move the wires during the tensioning process. Bronze jacking screws were used for final alignment during the tensioning process

on how to properly handle and install them. A 'mock-wire' installation was done to practice and identify the risks. After this, the actual wires were installed. The installation took approximately one week. The wires were installed serially, first the Y-plane, then the U-plane, and then the V-plane. After all the wires were installed, a G10 cover board was placed over carrier boards to secure and protect the electronics on the board, as shown in figure 3.5.

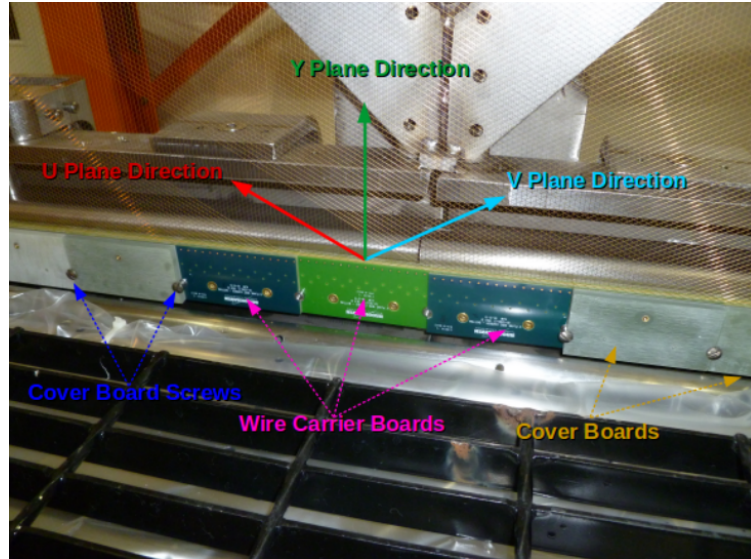


Figure 3.5: The MicroBooNE wires for 3 planes are shown here. The wire carrier boards are serially installed on the tensioning bar. The boards are held in place with a G10 cover plate that is secured with a smooth stainless steel screw.

449 Next, the wires were brought as close to nominal tension as possible. It was decided to
 450 favor under tensioning wires to minimize the risk of a broken wire during the tensioning
 451 process. The wire tensioning was done in a systematic way using the bronze jacking screws.

$$f = \frac{1}{2L} \sqrt{\frac{T}{\rho}} \quad (3.1)$$

452 Each wire has a characteristic resonance frequency that is related to its length, tension,
 453 and linear mass density through equation 3.1. A custom device was made to measure
 454 the resonant frequency of individual MicroBooNE wires. A laser light was focused on a
 455 particular wire and the wire gently plucked. A photo-diode mounted in an optical lens then
 456 measured the intensity of reflected light as the wire vibrated. The signals were then read into
 457 SpectrumAnalyzer, which is a software package that records frequency. SpectrumAnalyzer
 458 also allowed the high order frequency harmonics to be seen. The higher frequencies allowed
 459 for more precise tension measurement as see in Figure 3.6

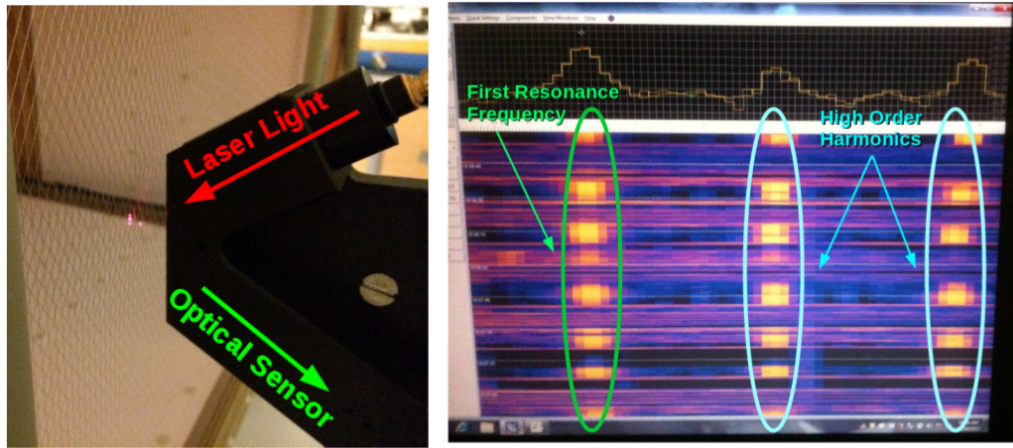


Figure 3.6: Left: Picture of the tension measuring apparatus including a laser and a optical sensor made of a photo-diode and a lens. Right: Example output of the SpectrumAnalyzer showing the first resonance frequency (bright line on the left) and the higher order harmonics (lines in the middle and left).

460 Note that the tension of 2328 out of 2400 U wires, 2308 out of 2400 V wires, and 3410
 461 out of 3456 Y wires was measured, corresponding to 97.5 % of all wires installed in the
 462 detector. Only the wires inaccessible to the tension measuring device were not measured.
 463 The average tension for U,V,Y planes respectively was 0.589 ± 0.012 kg, 0.664 ± 0.014 kg,
 464 0.525 ± 0.009 kg. The tension for each plane is shown in Figure 3.7 and Figure 3.8.

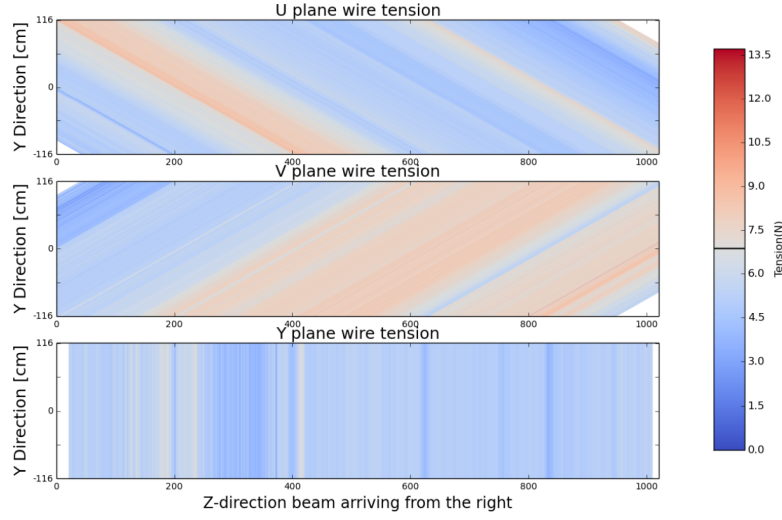


Figure 3.7: This a plane by plane map of the measured wire tensions for MicroBooNE.

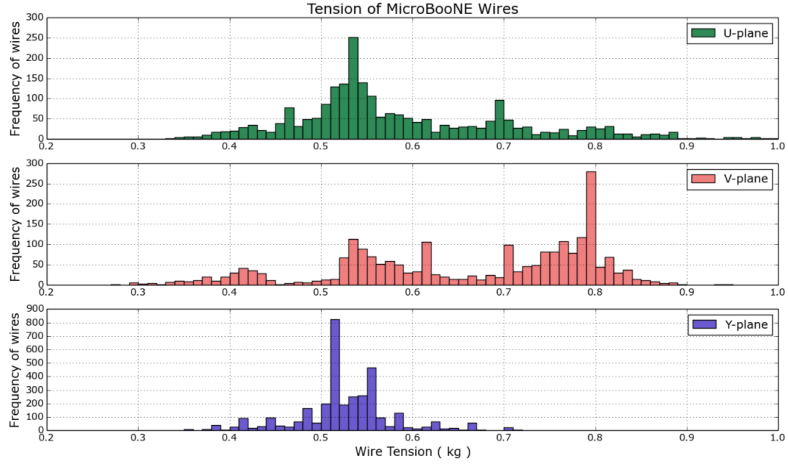


Figure 3.8: This a plane by plane histogram of the measured wire tensions for MicroBooNE.

3.4 Light Collection

The TPC can reconstruct 3D objects but there is still an ambiguity in the initial drift position. The light collection system in an LArTPC provides information to address this degeneracy. Scintillation light of liquid argon is 128nm wavelength and is produced through two primary reactions. The first, which accounts for $\approx 25\%$ of the light yield, is done through a Σ singlet excimer excitation and has a reaction time of 6 ± 2 ns. This type of

471 excimer is formed from an ionized argon atom that combines with another stable argon
 472 atom. The second, which accounts for the other 75% of light yield, is done through a Σ
 473 triplet excimer excitation and has a reaction time of $1590 \pm 100 \mu\text{s}$. The triplet state excimer
 474 is formed from a stable argon atom, an ionized argon atom, and a free electron.^[1] Since the
 475 prompt scintillation light is orders of magnitude faster than drift time from the TPC signal
 476 this information can be used to address this ambiguity.

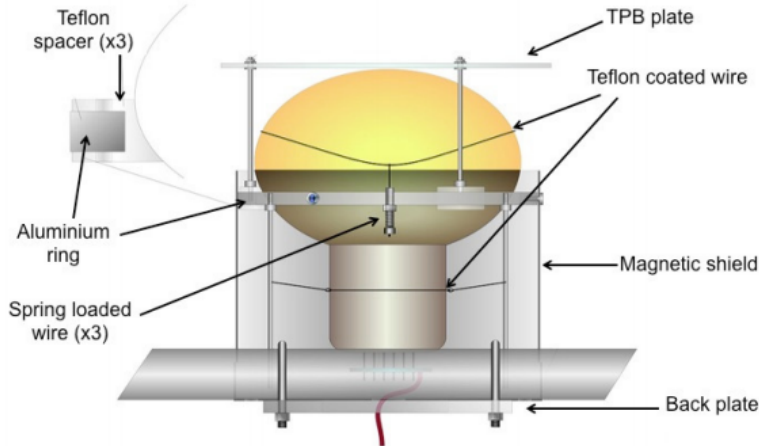


Figure 3.9: Schematic of a PMT optical unit for MicroBooNE.

477 The MicroBooNE light collection system consists of 32 8-inch diameter Hamamatsu
 478 R5912-02mod cryogenic PMTs. The PMT's are not optimized to detect 128nm vuv light.
 479 Therefore, an acrylic plate coated with tetraphenyl butadiene(TPB)^[2] was installed in front
 480 of the PMT's to act as a wavelength shifter. The TPB plate absorbs the 128nm light and
 481 re-emits it a peak wavelength of 425nm. Also, it is known that PMT response is reduced
 482 from certain orientations in the earth magnetic field. To address this a mu-metal shield was
 483 designed to extend just past the equator of the PMTs. A schematic of a PMT optical unit
 484 is shown in figure 3.9.

485 The PMT system is mounted on a railing behind the wire planes and spans the entire
 486 detector length as shown in figure 3.10. This also provides a weak handle on interaction
 487 position since the scintillation light is fairly localized. Most importantly, since MicroBooNE
 488 is a surface detector and constantly being bombarded by cosmic rays, the scintillation flash

489 is used as a method of identifying neutrino interactions coming in time with the beam.



Figure 3.10: PMT optical units installed on support racks inside the MicroBooNE cryostat

490 3.5 Electronics Readout

491 The TPC and PMT systems produce detector analog signals which need to be digitized,
492 transferred out of the detector, and written to disk through data acquisition(DAQ) software.
493 Both systems perform a first round of shaping and amplification in the cold LAr and then
494 interface with warm electronics for further processing. The DAQ continuously writes to disk
495 and creates a buffer which stores data for up to 24 hours. MicroBooNE employs various
496 triggers to signify beam and non-beam data blocks and permanently store data from the
497 buffer stream. A schematic overview of the TPC and PMT signal processing and readout
498 stages is shown in Figure 3.11.

499 For the TPC, a large portion of the electronics processing for the 8,256 wire signals
500 are performed directly in the LAr. To reduce electronics noise, the input distance from
501 the wires to the preamplifier is minimized. The sense wires directly interface with CMOS
502 analog front end ASICs which operate on cold motherboards. In total MicroBooNE has
503 516 CMOS ASICs. The ASICs generate 50 W of heat load which is a negligible impact on
504 the cryogenics system. The motherboards shape and amplify the low noise signal. There

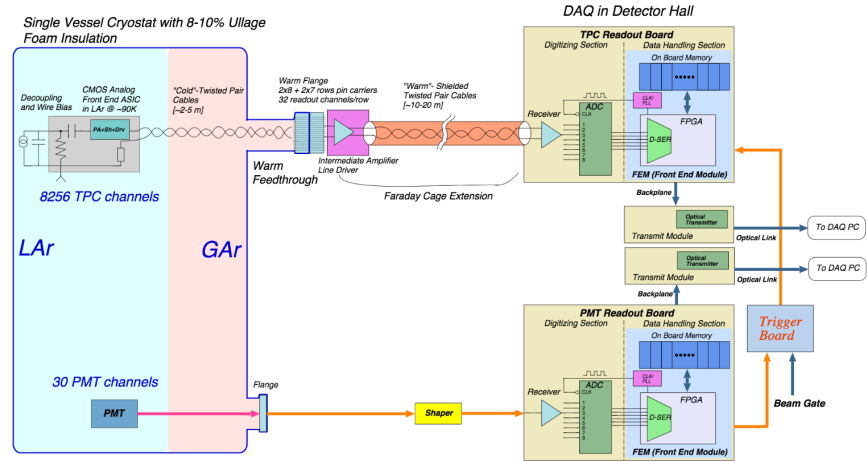


Figure 3.11: MicroBooNE LArTPC and PMT signal processing and readout schematic.

505 are 36 top style motherboards that instrument Y,U and V plane wires and 14 side style
 506 motherboards that instrument U and V plane wires. The signals are then passed through a
 507 series of 12 feedthrough ports to warm electronics. The warm signals are then distributed
 508 over nine readout crates, which digitize the signals.

509 The TPC system read out frame is defined to be 1.6 ms. This number was chosen
 510 to account for ionization electrons that are generated at the cathode and drift the entire
 511 distance to the wires in the presence of a 500V/cm E-Field. In MicroBooNE, an event is
 512 defined as four 1.6 ms readout frames. The additional frames allow for identification of
 513 cosmic particles that arrive before and after the neutrino interaction.

514 The PMT system is also processed in a similar fashion. The PMT's undergo 60 ns
 515 shaping to allow for precise measurements of the signal rising edge. The signals are sampled
 516 at 64MHz but only shaped signals above a threshold are read out and stored for data. The
 517 PMT signals are split into two different gains. A high gain signal that is 10 times the
 518 amplitude of the low gain. The signals are then brought to pre-amp/shaper boards and
 519 digitized and sent to the DAQ.

520 Chapter 4

521 Booster Neutrino Beam

522 Fermilab is one of the world's leading neutrino facilities and currently produces two neutrino
 523 beams that span a wide range of neutrino energies. The Booster Neutrino Beam (BNB),
 524 which will be described in detail throughout this chapter, is a lower energy beam that
 525 delivers neutrinos to various short baseline experiments. Fermilab also hosts the NuMI
 526 (Neutrinos at the Main Injector) Beam [] which produces neutrinos over a large range
 527 between 1GeV/c-30GeV/c and delivers neutrinos to various experiments both on-axis and
 528 off-axis. The NuMI beam will not be covered in this thesis.

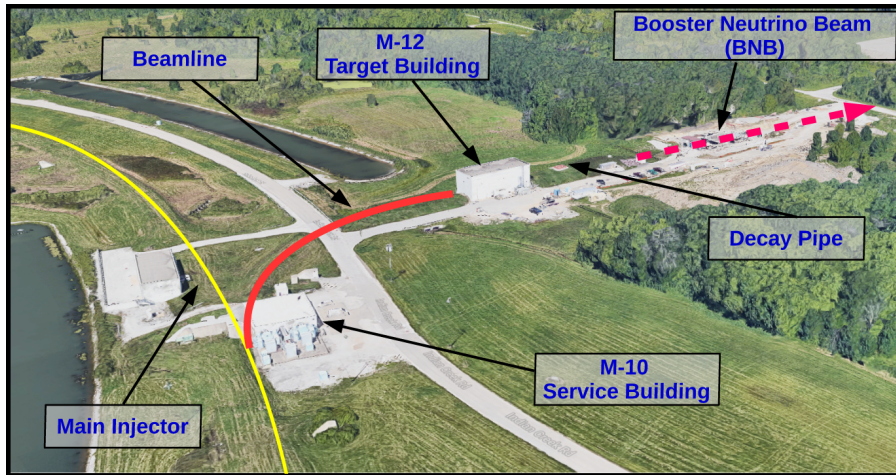


Figure 4.1: This image shows an aerial view of the Booster Neutrino Campus. Protons are extracted before the main injector near the M-10 service building and delivered to the M-12 target hall where the low energy neutrino beam is produced.

529 The Booster neutrino campus is illustrated in figure 4.1. To produce the BNB, protons
530 are extracted from a transfer line just prior to the main injector and then interact
531 with a beryllium target. The following sections will describe the beam system, neutrinoos
532 production process, and flux predictions for the BNB.

533 4.1 Primary Beam, Target and Horn

534 The BNB extracts 8.89 GeV/c momentum protons from the Fermilab Booster synchrotron
535 and delivers them to a beryllium target housed in the M-12 building. The protons from
536 the booster are grouped in 1.6 μ s windows called 'beam spills'. One beam spill contains
537 approximately 5×10^{12} protons. On average the Booster can run no more 5 Hz with no
538 more than 11 pulses in a row at 15 Hz. In optimal running conditions the Booster can
539 deliver 9×10^{16} protons on target (P.O.T) per hour.

540 The beam pipe directly leading to the target is approximately 5 feet long and is held
541 under vacuum to minimize proton interactions not originating from the target. The incom-
542 ing proton flux is measured by a pair of toroids which are positioned upstream of the target
543 and provide an error on P.O.T on the order of 2 %.

544 The target consists of 7 cylindrical beryllium slugs that together produce an effective
545 cylinder of 71.1 cm in length and 0.51 cm in radius. The use of multiple slugs gave the
546 beryllium more surface area to allow efficient heat transfer from a simple air cooling system
547 to be sufficient. An exploded view of the BNB target is shown in figure 4.2. As the protons
548 collide with the beryllium, large amounts of secondary and tertiary mesons, such as π^\pm, K^\pm ,
549 are produced . These mesons will later decay into neutrinos and other decay particles.

550 The target is positioned inside of a large toroidal electromagnet called a horn. The horn
551 is made of an aluminum alloy (6061 T6) and is pulsed with 174 kA of current to produces
552 a $1/R$ field where R is the distance from the axis of the horn. Since neutrinos are neutral
553 particles and can not directly be focused by an electric or magnetic force. Instead, the horn
554 focuses the proper sign parent π^\pm, K^\pm in such a configuration that the neutrino angle from
555 the parent decay particles are focused in a beam.

556 Directly downstream of the horn/target assembly is a collimator that is used to reduced

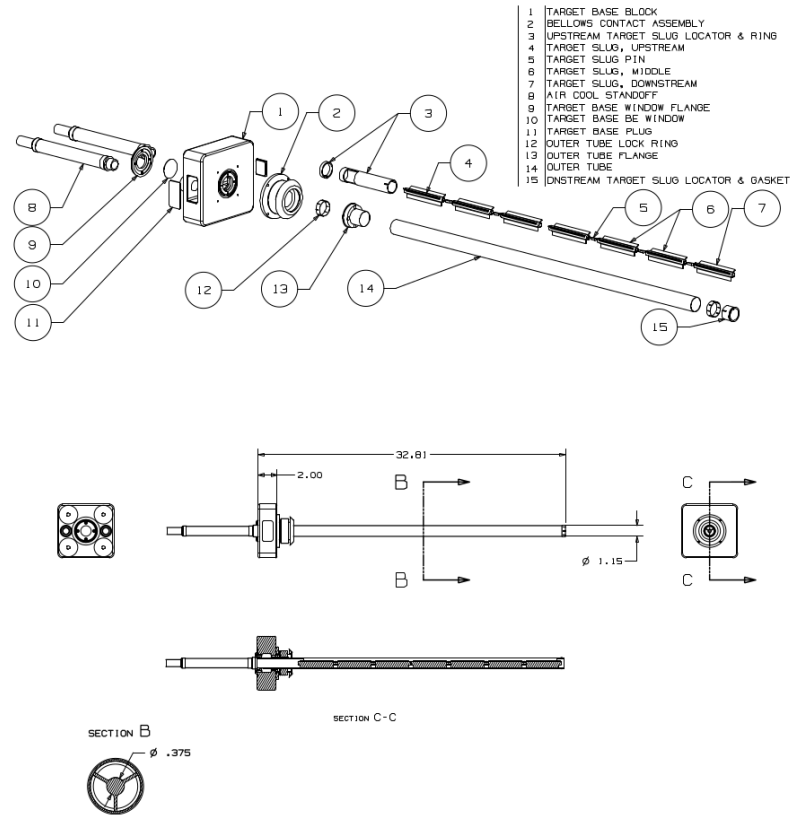


Figure 4.2: An exploded view of the BNB target which shows the 7 Beryllium slugs housed inside the support structure.

background coming from unwanted particles. Particles passing through the collimator enter a 45 m long decay region. In this region, most of the particles decay to produce the neutrino beam. At the end of the decay region there is a beam stop made of steel, concrete. There is also an array of gas proportional counters to detect high energy muons that punch through the beam stop. A diagram of the entire BNB system is shown in figure 4.3. When the horn polarity focuses (negative) positive charged mesons a (anti)neutrino beam is produced.

4.2 Neutrino Flux Prediction

The neutrino flux prediction for MicroBooNE uses the same GENIE simulation files used by MiniBooNE. The files are feed into a Geant4 module that simulates the particles as they

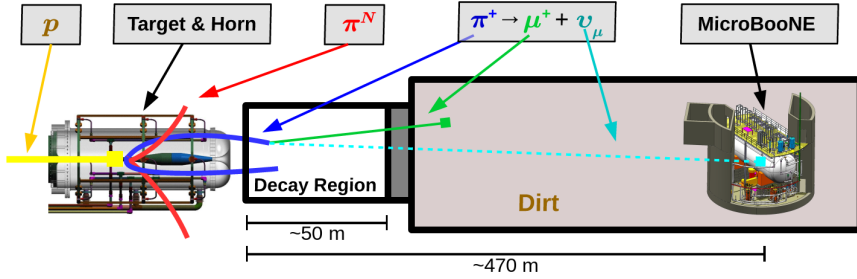


Figure 4.3: This figure shows the Booster Neutrino Beam line at FNAL. The neutrinos are produced in the decay region and then travel towards the MicroBooNE detector located 470 m down stream.

566 travel through the target, horn, and decay region. This produces a MC flux estimate for each
 567 of the various neutrino types. A systematics study was then performed to provide an error
 568 estimate for each of the ν_e , $\bar{\nu}_e$, ν_μ , and $\bar{\nu}_\mu$ flux predictions. To do this, 6 primary systematics
 569 were varied: the production rates of π^+ , π^- , K^+ , K^- , and K_L^0 , and a group systematic
 570 comprised of the horn current miscalibration, skin depth, nucleon inelastic, nucleon QE,
 571 nucleon total cross sections, pion inelastic, pion QE, and pion total cross sections. Beam
 572 errors for each of systematics are shown in Table 4.1 .The final flux estimate with the error
 573 uncertainty is shown in Figure 4.4.

	ν_μ	$\bar{\nu}_\mu$	ν_e	$\bar{\nu}_e$
Delivered P.O.T.	2.00%	2.00%	2.00%	2.00%
π^+	5.8%	0.46%	4.62%	2.66%
π^-	0.01%	7.51%	0.28%	3.20%
K^+	0.38%	0.13%	5.19%	2.61%
K^-	0.01%	0.35%	0.28%	3.92%
K_l^0	0.03%	0.27%	2.36%	22.59%
Other	5.78%	6.09%	3.6%	7.61%

Table 4.1: Systematic errors for production of various neutrino types with respect to their, P.O.T. , parent particle, and other variables.

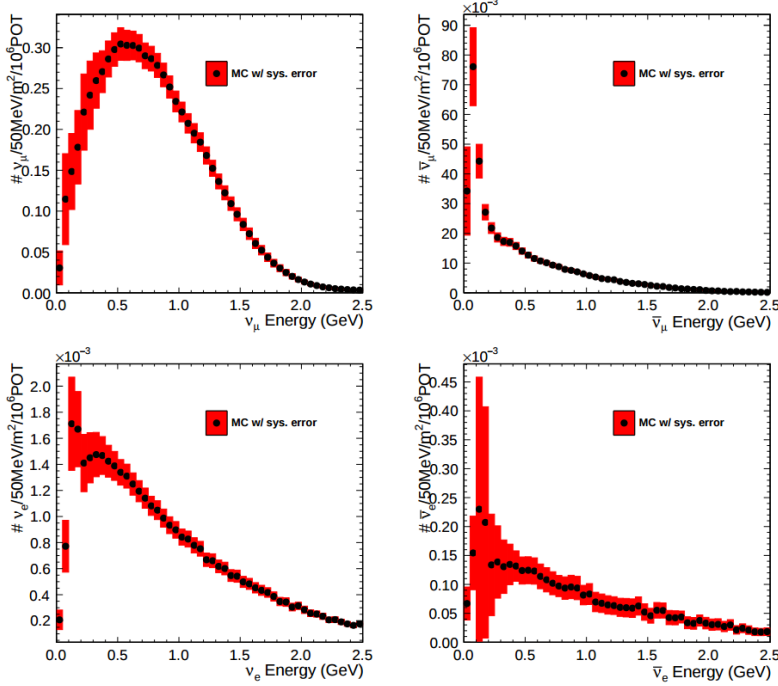


Figure 4.4: Monte Carlo flux predictions for the BNB neutrino spectrum. The red band represents the flux systematic errors. Note the orders of magnitude with the ν_μ spectrum rates.

⁵⁷⁴ Chapter 5

⁵⁷⁵ Low Energy Excess and Relevant ⁵⁷⁶ Cross Sections

⁵⁷⁷ 5.1 Overview

⁵⁷⁸ This chapter will discuss various facets of what is commonly called the “MiniBooNE Low
⁵⁷⁹ Energy Excess.” First, we will present the anti-neutrino excess observed by LSND and how
⁵⁸⁰ the oscillation results can be interpreted. Then, we will discuss the efforts of MiniBooNE to
⁵⁸¹ understand the LSND results along with their oscillation results that establish the “Mini-
⁵⁸² BooNE Low Energy Excess.” We will also discuss the neutral current $1\pi^0$ cross section
⁵⁸³ which is the dominant background in the oscillation analysis claims for both MiniBooNE
⁵⁸⁴ and LSND. Finally, we will discuss MicroBooNE’s role towards addressing understanding
⁵⁸⁵ the low energy excess claims of MiniBooNE.

⁵⁸⁶ 5.2 LSND Excess

⁵⁸⁷ The Liquid Scintillator Neutrino Detector (LSND) was a 167 ton neutrino detector stationed
⁵⁸⁸ at Los Alamos National Lab (LANL) designed to study neutrino oscillations. The detector,
⁵⁸⁹ which hosted 1220 PMT’s for event detection, was place 30 m away from the source of a
⁵⁹⁰ low energy (40 MeV) $\bar{\nu}_\mu$ beam. Using the Los Alamos LAMPF beam, 800 MeV protons
⁵⁹¹ interacted with a water target to produce π^+ mesons which decayed into $\mu^+ + \nu_\mu$. The μ^+

would then interact with a copper beam stop and decay at rest to produce the low energy $\bar{\nu}_\mu$ beam.

The detector medium was primarily carbon (mineral oil CH_2). LSND could easily distinguish between electromagnetic showers (electrons/positrons/photon) or tracks (pi- μ ons/muons/protons) by differences in the Cherenkov cone that was produced. The oscillation signal interaction was $p + \bar{\nu}_e \rightarrow n + e^+$. The primary e^+ is easily visible from the Cherenkov light it produced but a neutron will not produce Cherenkov light and therefore be invisible to the detector. The organic scintillator b-PDB was dissolved to the mineral oil at a concentration of 31 mg/l. The scintillator allowed the 2.2 MeV photon from the capture of the neutron on hydrogen to be detected. This allowed LSND a unique signal to identify $\bar{\nu}_e$ interactions. It should be noted that the detector technology could not easily discriminate between photons, electrons or positrons induced electromagnetic showers.

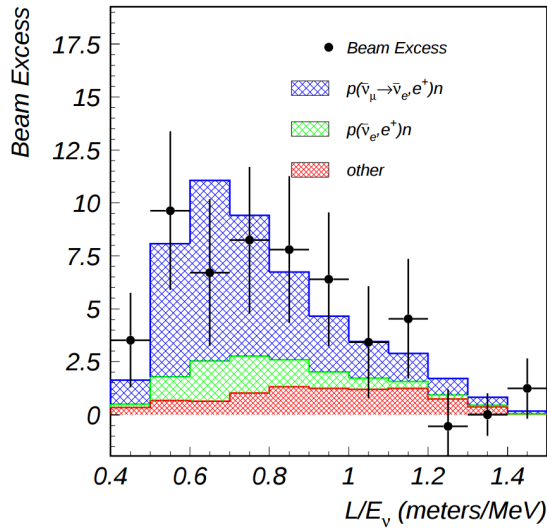


Figure 5.1: This is the LSND neutrino oscillation appearance plot as a function of L/E and represents the 87 event $\bar{\nu}_e$ excess claimed by the experiment.

604 In 2001, the collaboration published results for an observed excess of $87_{\pm 6.0}^{+22.4}$ events
 605 above the predicted background as shown in figure 5.1. If the excess is interpreted as
 606 neutrino oscillations from a two neutrino model, the best fit of the excess would suggest a
 607 $\sin^2(2\theta) = 0.003$ and $\Delta m^2 = 1.2\text{eV}^2$ which greatly contradicts many other measurements
 608 for $\Delta m_{2,3}^2$ or $\Delta m_{1,3}^2$ [1]. One explanation for the excess suggests the idea of mixing between
 609 other additional neutrino states. These neutrinos are called ‘sterile’ since they cannot
 610 directly couple via weak interaction as mentioned prior from the constraints from LEP.

611 5.3 Miniboone Excess

612 The Mini Booster Neutrino Experiment(MiniBooNE) was designed to address the claims of
 613 the LSND $\bar{\nu}_e$ excess result. The MiniBooNE detector was a mineral oil Cerenkov detector
 614 designed to be a similar technology to LSND. MiniBooNE, stationed at FNAL in the BNB,
 615 was positioned 541 m from the neutrino source and was able to receive both ν_μ and $\bar{\nu}_\mu$
 616 fluxes. The distance was chosen such that the L/E parameter were similar to that of the
 617 LSND experiment.

618 MiniBooNE, which contained 818 tons of mineral oil(CH_4), was located underneath
 619 more than 3m of earth overburden to help reduce cosmic rays. The detector supported a 35
 620 cm thick outer cosmic veto using 240 PMT’s. The veto efficiency was 99.99% for rejecting
 621 cosmic muons. The inside of the detector was instrumented with 1,280 8-inch PMT’s
 622 which were used to read out neutrino and comsic data. Cherenkov light from different
 623 particles produced distinct patterns on various PMT’s inside the spherical detector. A
 624 cartoon showing various type of signal topologies from the MiniBooNE detector are shown
 625 in figure 5.2. The detector energy scale was calibrated in situ by fitting various parameters
 626 from thoroughgoing muons, decay Michele electrons, and π^0 decays’s. A clear limitation of
 627 Cherenkov detectors is the inability to concretely distinguish between photon induced or
 628 electron induced showers.

629 The primary oscillation analysis for MiniBooNE was done ‘blind’ in an attempt to
 630 gain confidence from the physics community upon it’s findings. The entire analysis was
 631 developed on large statistics Monte Carlo simulation and a small sample of test data. In

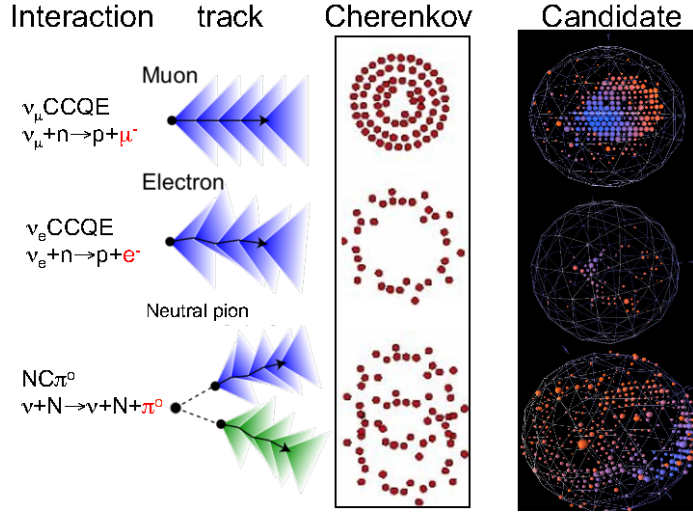


Figure 5.2: This cartoon depicts different particle interactions as observed in Cherenkov detector. The far right shows the interaction types as viewed in MiniBooNE

total, MiniBooNE accumulated 6.46×10^{20} P.O.T. of ν -data and 11.27×10^{20} P.O.T. of $\bar{\nu}$ -data. Fermilab's ability to support both neutrino and anti-neutrino beams allow for MiniBooNE to confirm that an LSND-like excess was independent of neutrino type. The data is in good agreement between signal and background predictions and contradicts the LSND claim up to 98% confidence in both modes above 500 MeV. The excess is most prominent in the region of events below 500 MeV, as seen in figure 5.3. In this region the largest background comes from π^0 -misidentification followed by photons coming from radiative Delta decays. MiniBooNE reports a total excess of 240.0 ± 62.9 combine $(162.0 \pm 47.8\nu, 78.4 \pm 28.5\bar{\nu})$ events in the neutrino energy range $200 < E_\nu^{QE} < 1250$ MeV. Also, if the excess is interpreted as a two flavor oscillation the inferred parameters are consistent with the LSND result.

5.4 Neutral Current π^0 production

The leading background from the MiniBooNE oscillation result, as mentioned in chapter 5.3, is π^0 -misidentification. Accurately measuring the neutrino induced neutral current single π^0 production cross section is therefore crucial in understanding background contributions for an oscillation analysis. Charge current π^0 production conveniently has an outgoing

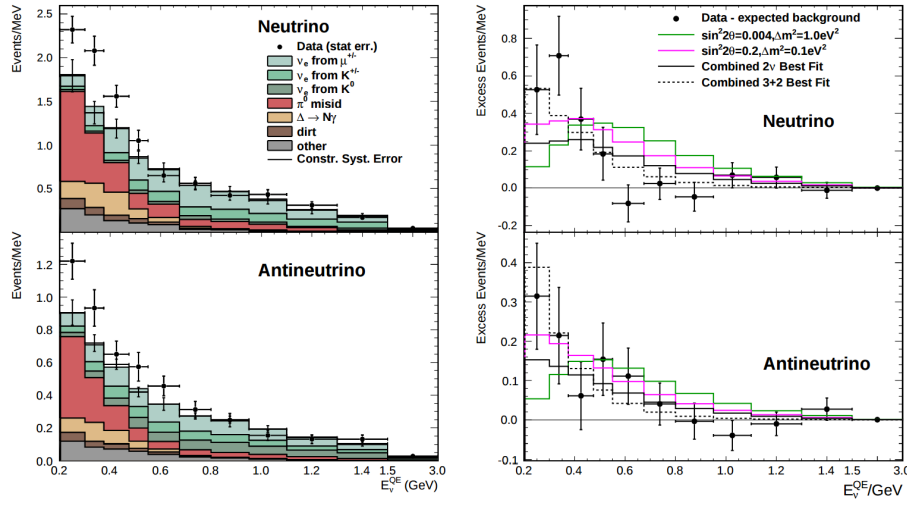


Figure 5.3: The left plots show the stacked histograms for signal and background overlaid with data for both neutrino and anti-neutrino modes. The right plots show the relative excess as a function of neutrino energy and make obvious the energy range that drives the excess.

647 charged muon in the final state and is very easy to identify. On the other hand, neutral
 648 current π^0 production does not guarantee any outgoing charged particles and therefore,
 649 makes identification much harder. For neutrinos in the BNB, the main production mode
 650 for neutrino induced neutral current π^0 production is via the $\Delta(1232)$ resonant production.
 651 Resonant production is when a baryon, such as a proton or neutron, are excited to a higher
 652 resonance state and then subsequently decays back to the initial state while liberating a
 653 π^0 . There are other neutrino induced π^0 production modes that MicroBooNE is sensitive to
 654 such as deep inelastic scattering and coherent production, but have a lower production cross
 655 section at the given BNB neutrino energy range. A general Feynman diagram can be used to
 656 describe the main components of neutrino induced neutral current single π^0 production in
 657 argon as seen in Figure 5.4.

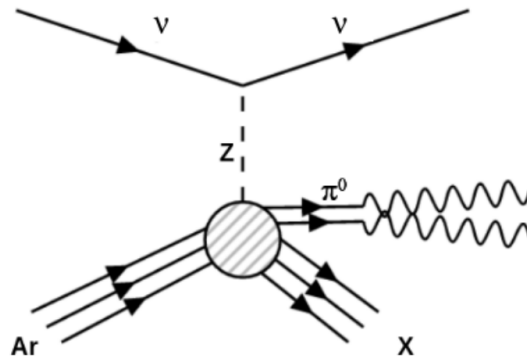


Figure 5.4: Neutrino induced single π^0 production on argon. This topology is defined such that 1 π^0 is produced and the other particles leaving the interaction (X) must only consist of nucleons.

658 5.5 NC-Pi0 in Carbon vs Argon

659 In 2010, MiniBooNE measured the total neutral current single π^0 cross section on carbon
 660 with what is currently the worlds largest statistics sample of π^0 s. The MiniBooNE neutral
 661 current single π^0 signal is defined as a topology that produces one and only 1 π^0 in the
 662 final state with no other other charged leptons or mesons originating from the vertex. In
 663 2015, the first measurement of neutrino induced neutral current π^0 production on argon was
 664 measured by ArgoNeut collaboration at Fermilab while running in the NuMI neutrino beam.
 665 AgroNeut, being a smaller detector, could not easily contain many of the electromagnetic
 666 showers from π^0 decays. This forced the analysis choose a slightly different final state signal
 667 definition requiring there to be at least one π^0 , no electron or muon, and allowing there
 668 to be any number of mesons in the final state. This modified signal definition makes any
 669 comparison to other historical data very complicated.

670 MicroBooNE, which resides in the same neutrino beam line as MiniBooNE, is a prime
 671 candidate for various studies of neutral current π^0 production studies between different
 672 target materials(C/Ar). Being a larger LArTPC, more π^0 decays will be contained allowing
 673 for high statistics measurements of the cross section along with the general need to measure
 674 the production rate as input to its own oscillation analysis.

675 Chapter 6

676 Cosmogenic π^0 's at MicroBooNE

677 In this chapter we will talk about some of the challenges and interesting physics cases re-
678 garding cosmogenics in a surface LArTPC. Many cosmic ray particles penetrate surface
679 detectors and populate the detector region making it necessary to remove these particles
680 from reconstruction and address charge contamination in neutrino events. The majority
681 of this chapter will emphasize cosmogenic track removal, electromagnetic showers and sub-
682 sequently π^0 selection. We will first examine some historical cosmogenic studies from the
683 Icarus experiment. Then, introduce what MicroBooNE can contribute in terms of under-
684 standing cosmics. We will address the cosmic simulation that is used, various steps in
685 reconstruction and pattern recognition used to select π^0 's in a LArTPC. Finally, we will
686 conclude with how these studies impact future cross section analyses and backgrounds to-
687 ward the low energy excess analysis.

688 6.1 Motivation

689 Cosmogenic particles allow for the separate test of reconstruction tools along with an inde-
690 pendent way to address the detector energy scale. The high rate of surface cosmics cause
691 some trouble with disentangling signal neutrino events so cosmic ray removal. Luckily, off
692 beam surface cosmogenic samples allow for a large statistics dataset to develop and optimize
693 reconstruction techniques. Cosmogenic muons that traverse the detector provide a handle to
694 understand detector energy scale along with understanding track reconstruction efficiency.

695 Stopping muons that produce a Michele electron help provide a benchmark for low energy
 696 showers in the 10's of MeV range. The π^0 resonance, with a mass of $134.9 \text{ MeV}/c^2$, can be
 697 used as a standard candle to benchmark overall detector energy scale. The calculate the π^0
 698 mass, as shown in equation 6.1, depends on a measurement of energy and photon opening
 699 angle.

$$\mathcal{M} = \sqrt{2E_1E_2(1 - \cos\theta_{12})} \quad (6.1)$$

700 Electromagnetic shower reconstruction for LArTPC's is well known to be a hard task.
 701 The high resolution of the 2-dimensional projections of EM-showers introduce many chal-
 702 lenges to develop unbiased and fully automated reconstruction. In 2001, the T600 ICARUS
 703 detector ?? performed a surface test run in Pavia, Italy. During this 100 day test the detec-
 704 tor collected over 30,000 cosmic ray events. In 2008, the ICARUS collaboration published
 705 a study of electromagnetic showers coming from π^0 decays in the Pavia dataset. To select
 706 candidate π^0 events, ICARUS hand scanned a total of 7,500 potential events from a PMT
 707 triggered sample. Their hand scanning requirements included, that at least two well sep-
 708 arated electromagnetic showers were visible, a valid t_0 time for the vertex, and that there
 709 was not much charge contamination coming from a nearby cosmic muon. After this, they
 710 were left with 212 hadronic interactions with at least one candidate neutral meson' which
 711 they then proceeded to reconstruct. Their final reconstruction consisted of energy scaling
 712 to account for missing charge in the shower and a minimization against the true π^0 mass
 713 (134.9). An example of one of their hand scanned clustering events is shown in Figure 6.1.

714 MicroBooNE, being a surface detector, is in a position to do a similar study with im-
 715 proved reconstruction techniques. Also, understanding the cosmic production rate for single
 716 π^0 's is valuable to any MicroBooNE analysis that involves EM-showers. The following sec-
 717 tions will present MicroBooNE's Monte Carlo simulation and state of the art reconstruc-
 718 tion techniques.

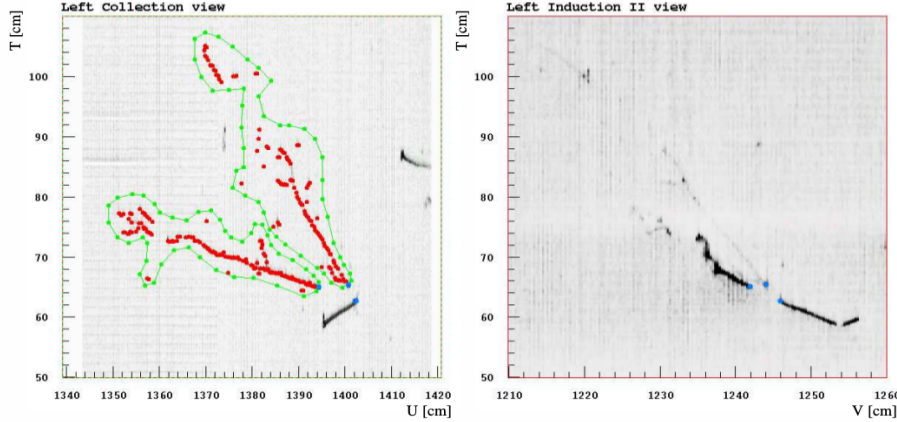


Figure 6.1: A cosmic π^0 from the ICARUS Pavia run. The left image, shows the hand drawn clustering and positions of the shower conversion point and vertex point. The right image, shows the same event on a different wire plane view.

6.2 Traditional Reconstruction

The traditional approach for LArTPC reconstruction involves grouping drift charge that is deposited on the wires to form wire-hits. The light collection system also has light-hits which corresponded to collected light of an individual track or shower. A group of PMT's that have light-hits at the same time is called a flash. Hits from each of the wire planes are clustered together with various reconstruction algorithms to form reconstruction objects that relate to individual particles in the detector. There are two primary reconstruction objects: tracks, which are mostly linear and compact clusters that represent muons, protons, and charged pions, and showers which are more fuzzy shaped cluster objects that represent photons and electrons. Next, to reconstruction a 3D object, an algorithm must match the same 2D cluster objects in at least two of the three wire planes. For MicroBooNE, and the general LArTPC community, matching track reconstruction is well advance but shower reconstruction suffers many hurdles. In recent years lots of progress has been made for LArTPC shower reconstruction. Various different techniques such as: improved 2D clustering and matching techniques[], sophisticated pattern recognition tools[] , and deep learning[] approaches have been explored and each has it's various strengths and weaknesses.

⁷³⁵ **6.3 Wire Cell Imaging**

⁷³⁶ The traditional approach is not the only way to reconstruct LArTPC data. Instead, wire
⁷³⁷ data can be treated with a tomographic approach directly producing a set of 3D space
⁷³⁸ points. Although computationally intensive, this approach allows for more information to
⁷³⁹ be used in a 3D clustering framework which can directly impact shower reconstruction and
⁷⁴⁰ mitigate degeneracies from the 2D matching method.

⁷⁴¹ The Wire-Cell framework, spearheaded by Brookhaven National Labs (BNL), utilizes
⁷⁴² this approach to create 3D space points from MicroBooNE's TPC data. The approach
⁷⁴³ relies on the assumption that the same amount of ionization charge is seen on each plane.
⁷⁴⁴ In MicroBooNE this is done by reconstructing small time slices on each wire planes. Each
⁷⁴⁵ time slice involves solving a charge equation for all possible hits with respect to the matrix of
⁷⁴⁶ hits actually recorded in the time slice. The charge equation is shown in equation 6.2. The
⁷⁴⁷ detector wire signals are represented in matrix W while all potential wire hits are contained
⁷⁴⁸ in H. Nonzero values in the Q matrix will correspond to unique wire-plane intersections of
⁷⁴⁹ charge, near zero values represent ghost hits due to degeneracies in the charge equation.

$$\begin{bmatrix} W_{u_1} \\ \vdots \\ W_{u_n} \\ W_{v_1} \\ \vdots \\ W_{v_n} \\ W_{y_1} \\ \vdots \\ W_{y_n} \end{bmatrix} = \begin{bmatrix} Q_{u_1}^{H_1} & Q_{u_1}^{H_2} & \dots & \dots & \dots & Q_{u_1}^{H_{m-1}} & Q_{u_1}^{H_m} \\ \vdots & \vdots & \ddots & \ddots & \ddots & \vdots & \vdots \\ Q_{u_n}^{H_1} & Q_{u_n}^{H_2} & \dots & \dots & \dots & Q_{u_n}^{H_{m-1}} & Q_{u_n}^{H_m} \\ Q_{v_1}^{H_1} & Q_{v_1}^{H_2} & \dots & \dots & \dots & Q_{v_1}^{H_{m-1}} & Q_{v_1}^{H_m} \\ \vdots & \vdots & \ddots & \ddots & \ddots & \vdots & \vdots \\ Q_{v_n}^{H_1} & Q_{v_n}^{H_2} & \dots & \dots & \dots & Q_{v_n}^{H_{m-1}} & Q_{v_n}^{H_m} \\ Q_{y_1}^{H_1} & Q_{y_1}^{H_2} & \dots & \dots & \dots & Q_{y_1}^{H_{m-1}} & Q_{y_1}^{H_m} \\ \vdots & \vdots & \ddots & \ddots & \ddots & \vdots & \vdots \\ Q_{y_n}^{H_1} & Q_{y_n}^{H_2} & \dots & \dots & \dots & Q_{y_n}^{H_{m-1}} & Q_{y_n}^{H_m} \end{bmatrix} \begin{bmatrix} H_1 \\ H_2 \\ \vdots \\ H_{m-1} \\ H_m \end{bmatrix} \quad (6.2)$$

750 Then, each ‘slice’ is stacked to it’s corresponding x position. This produces a set of 3D
751 space points that can used in patter recognition algorithms to identify different particles
752 in the data. All reconstruction is done with accounting for known detector dead regions.
753 The current state of MicroBooNE’s signal and noise processing and imaging that requires
754 a minimum of 2 wire planes to be matched from the charge equation.

755 **6.4 Pattern Recognition**

756 Various pattern recognition tools are needed to address MircoBooNE’s TPC data but for
757 this analysis they can be generalized into two efforts, cosmic track removal and EM-shower
758 clustering. Both approaches require different techniques. First, we will focus on optimizing
759 track removal. This involves identifying tracks that are thoroughgoing, and contained. Once
760 all the charge associated with tracks are removed, the remaining charge is clustering into
761 candidate EM-shower objects. Finally, correlated shower pairs are identified and selected
762 as candidate π^0 events.

763 A image of a typical MicroBooNE cosmic event reconstructed with 3D wire cell space
764 points are shown in Figure 6.2 using the BEE viewer []. A detailed list of reconstruction
765 and selection parameters are listed in appendix ??

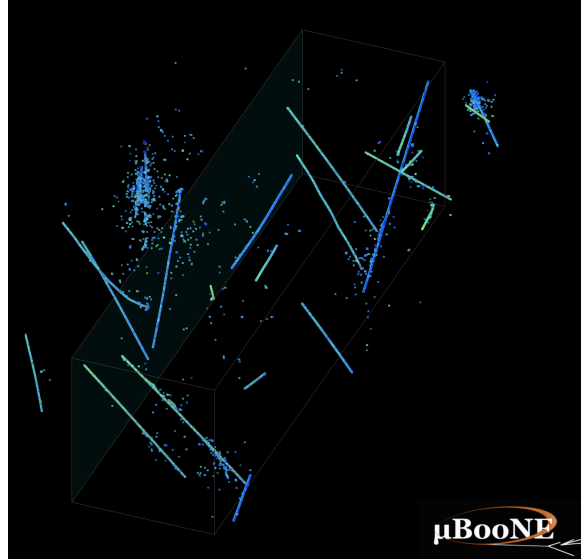
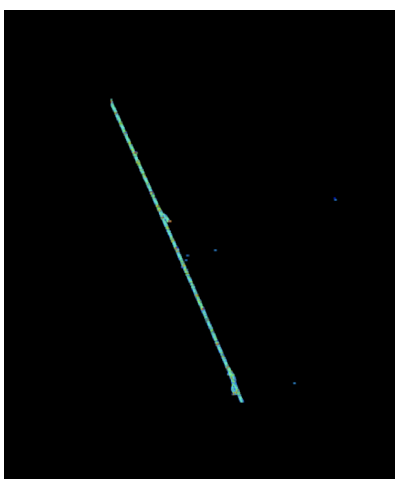


Figure 6.2: This is a typical cosmic event in the MicroBooNE detector. The data used to generate this event is CORSIKA MC.

766 6.4.1 Clustering

767 The wire cell data produces a set of 3D space points as mentioned in section 6.3. Only space
 768 points that are in the fiducial volume are clustered and considered in the reconstruction
 769 process. First a threshold cut of 500 Q is applied to all the remaining space points. This
 770 is done to remove very low charge ghost points and reduce the overall number of points to
 771 cluster. The main goal of this step is to identify the large scale structure of the cosmic
 772 tracks in the data. Additionally, with a smaller number of space points the computational
 773 time for reconstruction is reduced.

774 The first stage of clustering uses BIRCH (balanced iterative reducing and clustering
 775 using hierarchies). The hyper parameters were tuned such that cosmic tracks are removed
 776 with minimal impact to showers involved from π^0 . Birch clustering was chosen because it
 777 scales well with large number of points, efficiently maintains large number of clusters in
 778 datasets and also handles outliers removal well. This clustering technique leverages on
 779 the inherent structure of track like particles having a well defined 3-dimensional trajectory.
 780 Particles such as protons, muons, and charged pions are continuously ionizing meaning
 781 that there should be no gaps in the detected charge. This feature is much different than



(a) This figure shows an image of muon track as viewed from the BEE-WireCell image viewer.



(b) This figure shows an image of $\pi^0 \rightarrow \gamma\gamma$ decay as viewed from the BEE-WireCell image viewer.

782 EM-showers which have lots of gaps between detected charge. An example of this is shown
783 in figure ??

784 The next stage of the track and shower clustering process is to merge together proto-
785 clusters that did not get fully grouped together in the BIRCH clustering step. The second
786 pass clustering is geared toward larger object clustering. To address this, a 3D convex hull
787 is constructed around every cluster. Next, the euclidean distance between all the vertex
788 points calculated. If the minimum merging distance is small, the clusters from tracks get
789 merged together well. Clusters from showers still need further.

790 The final stage of clustering is shower clustering. This requires there to be a distinction
791 between a cluster object that is shower-like or track-like. To do this, parameters that
792 describe various aspects of a cluster are calculated. The most important features from
793 the cluster parameters are cluster length and spread of the first principle component. More
794 details about track and shower selection are described later in section 6.5.

795 Once defined as a shower cluster, a 3D charge weighted axis is fit to the cluster's set
796 of space points. First, a distance of closest approach (DOCA) for each cluster axis pair
797 is calculated and a proto-vertex is calculated at the midpoint of the DOCA line. Next,
798 a unique conversion point is calculate for each shower pair to identify the start point of

799 the shower. This can also be thought of as a proxy for the photons conversion point. Using
 800 the prot-vertex point and two conversion points an opening angle is calculated. A pair of
 801 clusters that have a DOCA that is less than 5 cm, an angle between 15 and 165 degrees,
 802 and both of the conversion lengths are less than 20 cm are merged together. The merging
 803 is done for all shower cluster pairs.

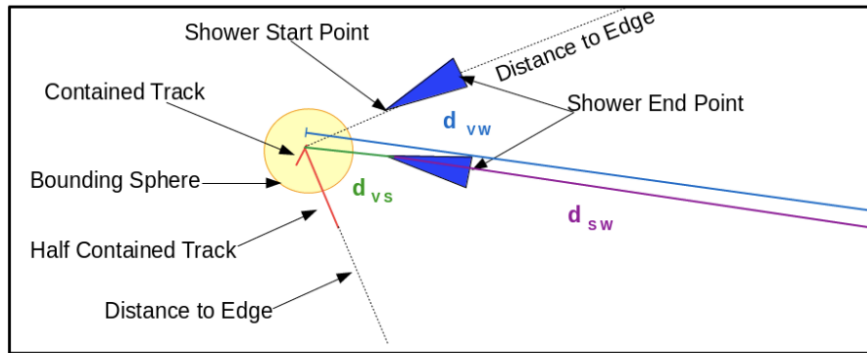


Figure 6.3: This graphic illustrates all the data objects and relevant parameters. The shower objects are shown in blue, track objects shown in red, and a bounding sphere, used to associate tracks with the vertex, is shown in yellow.

804 6.5 Track and Shower Selection

805 6.5.1 Track Removal

806 For this analysis track removal is handled in a unique manner. The primary goal is to
 807 identify showers coming from a π^0 . Therefore, all cuts and optimizations will be teste
 808 d against shower objects. The general approach for track removal depends heavily on
 809 geometric properties such as length and linearity of the cluster.

810 6.5.2 Single π^0 Reconstruction

811 The vast majority(98.8%) of π^0 's decay into two photons. The relationship for the par-
 812 ticle mass, which was defined in eq6.1, shows the importance of properly accounting for
 813 the energy and angle between the decay photons. To understand a baseline for reconstruc-

tion efficiency we have generated a sample of 10,000 single particle π^0 events isotropically throughout the detector volume with initial momenta spanning from 0 to 2 GeV.

First we will investigate energy deposited in detector from the decay. An plot of the true kinematic energy of photons from the decay particle is shown in Figure 6.4. It is important to note that both photons need to be reconstructed to form a resonant mass. This means that we are driven to optimize the reconstruction to be robust around showers in the range of many 10's of MeV in deposited energy. Photons that convert near the fiducial edge of the detector can escape and deposit only a small amount of energy in the detector. This poses problems for capturing the total amount of energy of the shower and drives the need for a fiducial cut around the edges.

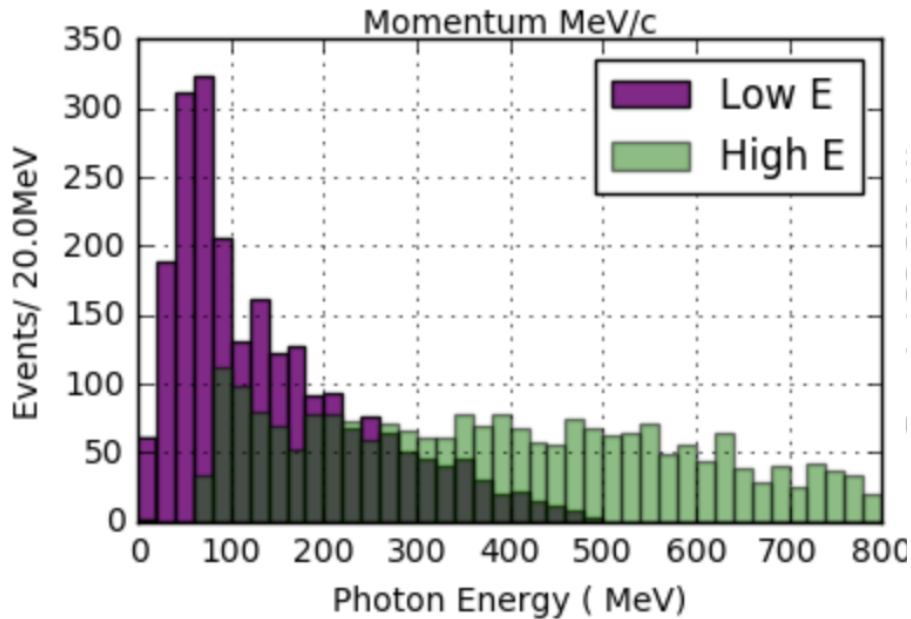
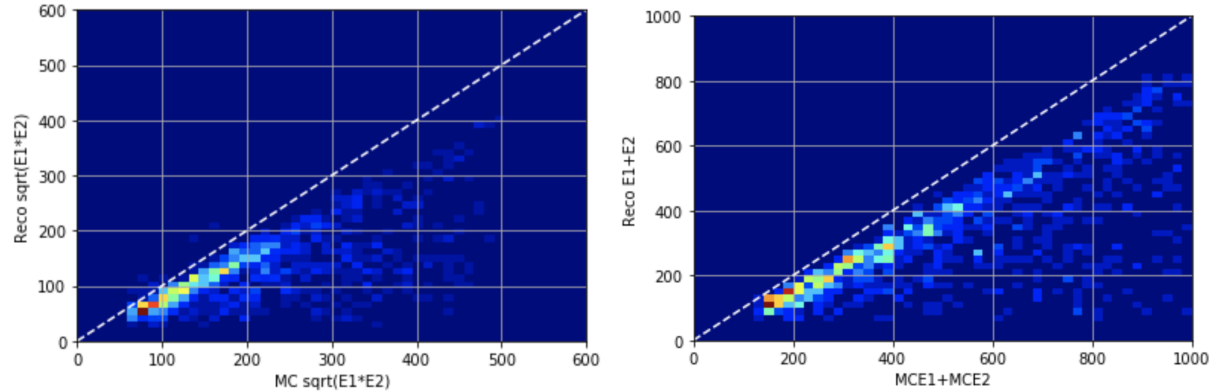


Figure 6.4: This figure shows the photon distribution for π^0 decays from a single particle sample of between 0-2GeV. The higher energy photon is shown above in green along with the corresponding lower energy photon shown in magenta.

To understand the reconstruction accuracy for the energy we are most interested in two metrics. The first is the total collected energy deposited by the two showers. This informs us that we are accounting for most of the energy deposited and handling the fiducial cuts



(a) Scatter plot of reconstructed energy sum vs true energy sum
(b) Scatter plot of reconstructed energy product vs true energy product

Figure 6.5: Reconstructed energy sum and energy product for shower pairs. Both, the reconstructed energy sum and product is less than the true energy deposited.

well. The second is the product of the two shower energies. This directly impacts the reconstructed mass resolution and informs us that we are properly clustering energy between the two showers properly. In figure 6.5 both metrics are plotted for reconstruction against true. Points along the diagonal would represent accurate model predictions. As we will see later in this chapter, the energy product drives the width of the mass resolution.

Next we will investigate the effects of the opening angle between the two photons. The minimum opening angle of the photons is constrained by the momentum boost as the particle decays as shown in equation 6.3. The angular resolution is a very challenging problem in LArTPC's using the traditional 2D projection approach. Fortunately, direct 3D reconstruction improves the angular resolution and allows for a better measurement of shower direction.

$$\sin \frac{1}{2} \theta_{min} = \frac{M}{E_{\pi^0}} \quad (6.3)$$

A plot of the reconstructed vs true opening angle is shown in Figure 6.6. The $1 - \cos\theta$ term from equation 6.1 is sensitive to tails of the mass distribution.

Next, we apply a final set of selection cuts. First, we require that the distance of closest

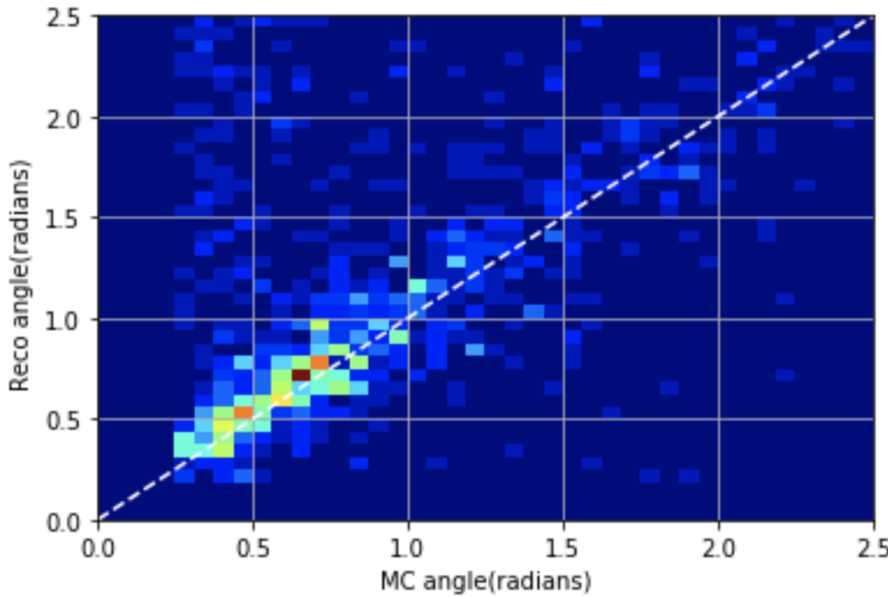


Figure 6.6: This scatter plot shows the reconstructed opening angle vs. true opening angle. We see that the reconstruction does very well with reconstructing this quantity due to the use of wire-cell's 3D approach. When the reconstruction performs badly it tends to identify small opening angles as large ones since we are not using any vertex information.

approach between the two shower axis is less than 5 cm. This is to help ensure that the photons are originating from a common origin. Next, the photon conversion distance can not be longer than 70 cm. This is done to help identify showers that are correlated from the same decay. Finally we only accept showers that are above 50 MeV in reconstructed energy. Figure 6.7 shows the effect of various parameters as applied to the reconstruction. We find that the deficit in mass peak is mainly due to the energy reconstruction. This is due to the missing energy during clustering . For this analysis there is also an additional component of energy missing since we will not be using the initial t_0 -tag. Without using t_0 , there is no effective way to correct back for electron drift effects. Thankfully, this effect is can be captured in understanding the distribution of reconstructed mass peak in the Monte Carlo.

Finally, we address the over all efficiency for reconstruction. The average reconstruction efficiency between 0 and 1 GeV/c is 40.1%. The reconstruction efficiency is shown in Figure 6.8. As can be seen there, the efficiency drops at low and high energies. At low momentum

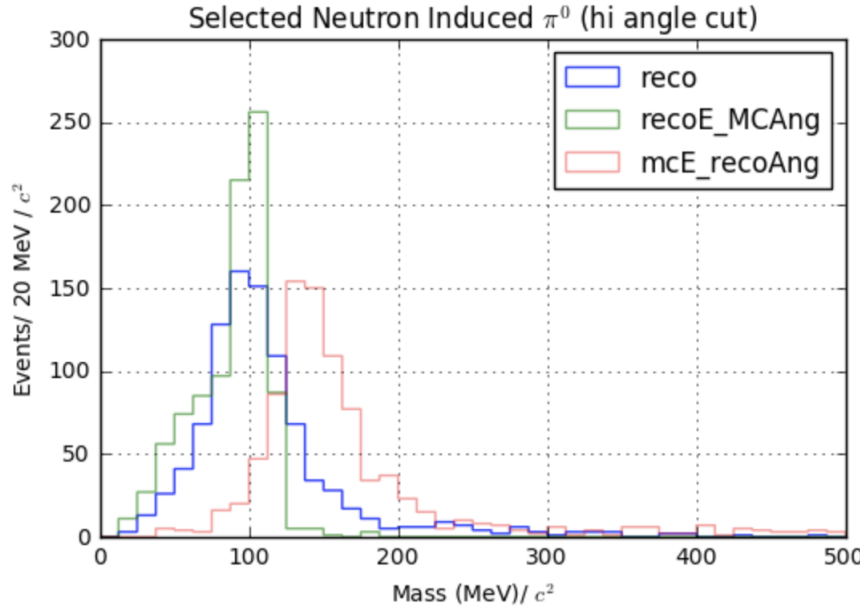


Figure 6.7: The reconstructed mass distribution is shown to highlight effects from reconstruction. First, in blue, the full reconstructed mass is shown. Second, in green, the reconstructed mass is calculated using the true angle. Third, in red, the reconstructed mass is calculated using the true energy.

the π^0 's are produced nearly at rest with both showers having similar energies. Most importantly the showers are produced nearly back to back. Without having a well defined vertex, sometime the reconstruction will identify the angle as being close to zero. Being that there is a minimum opening angle cut some of the events are lost from this effect. At high momentum, many of the showers are boosted to small opening angle which we see a similar effect in the loss of efficiency.

6.6 Single π^0 cosmic sample

The MicroBooNE cosmics Monte Carlo is generated by CORSIKA(COsmic Ray Simulation for Kascade) v-7.4003[?] CORSIKA simulates particles coming from a wide range of interactions initiated by cosmic ray particles in the upper atmosphere. The simulation is robust and accounts for various input parameters such as, longitude and latitude, elevation,

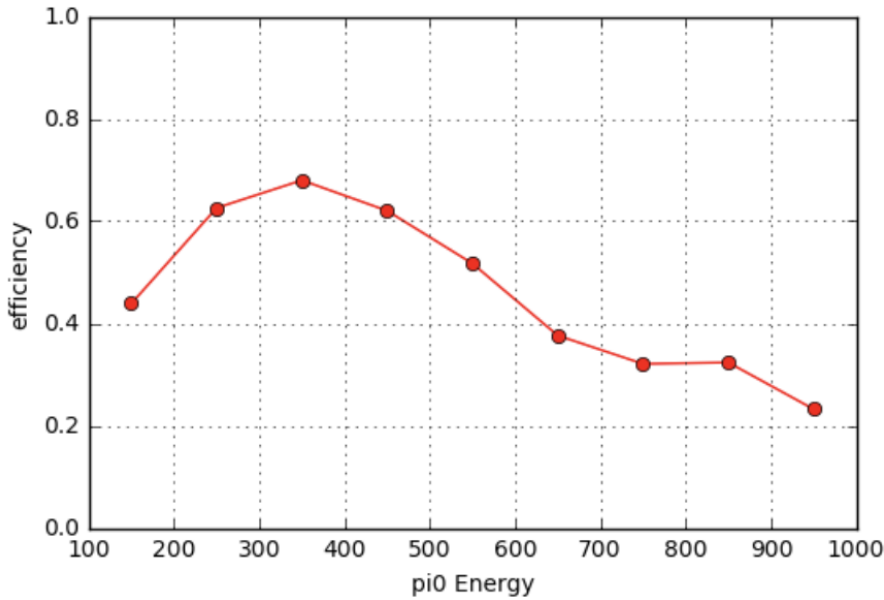


Figure 6.8: The plot shows the π^0 reconstruction efficiency for π^0 's over a 1000-10,000 MeV energy range. The reconstruction efficiency peaks around 350 MeV which conveniently is around the production energy for cosmic π^0

and the earth's magnetic field. The particles are simulated over a large region above the detector complex but only particles that travel through the detector cryostat volume are kept. The passage of these particles simulated by the GEANT4 package. Cosmic rays that do not travel through the cryostat have a low likelihood of producing secondary or tertiary particles that enter the detector TPC volume[?]

In one MicroBooNE drift window(2.3ms) there are on average 6 cosmic muons. The muons do not directly contribute to many EM-showers but sometimes pass through an EM-shower from another particle. For MicroBooNE, the vast majority of muons are through going and do not lead directly to any method of π^0 production.

Various other particles such as, protons, neutrons, and charged pions enter the TPC volume and may produce π^0 's. A distribution of π^0 production process is shown in Figure 6.9. Nearly half of the π^0 's produced in the MicroBooNE TPC are produced through a neutron inelastic scattering.

In total, 100K corsika truth events were produced to constrain production rates for signal and background. From that, a random sample of $\tilde{10}$ K events were ran through the wire-cell imaging reconstruction. Additionally, a signal sample of $\tilde{1.2}$ K was produced and reconstructed through the wire-cell imaging. *The exact rates will be discussed in Chapter 7.

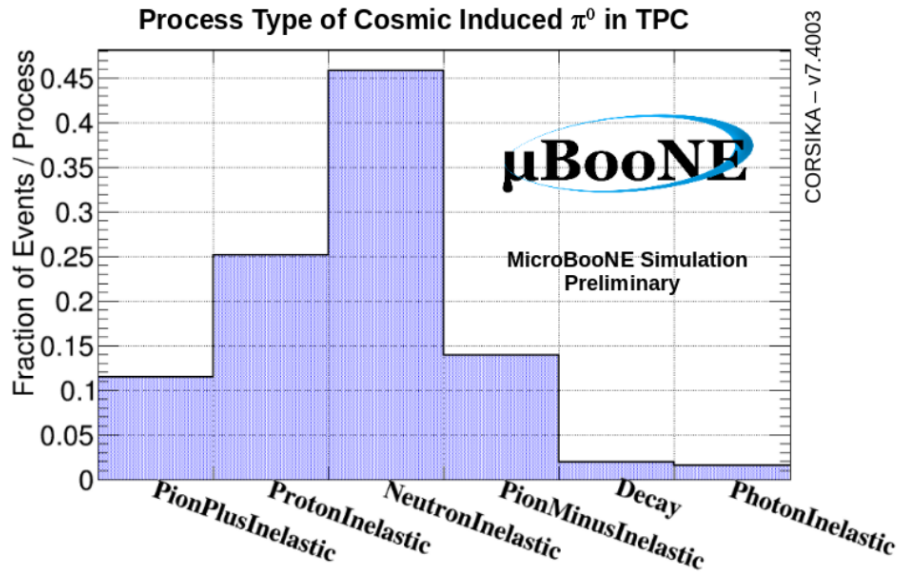


Figure 6.9: Physical process for cosmic π^0 that decay inside the TPC.

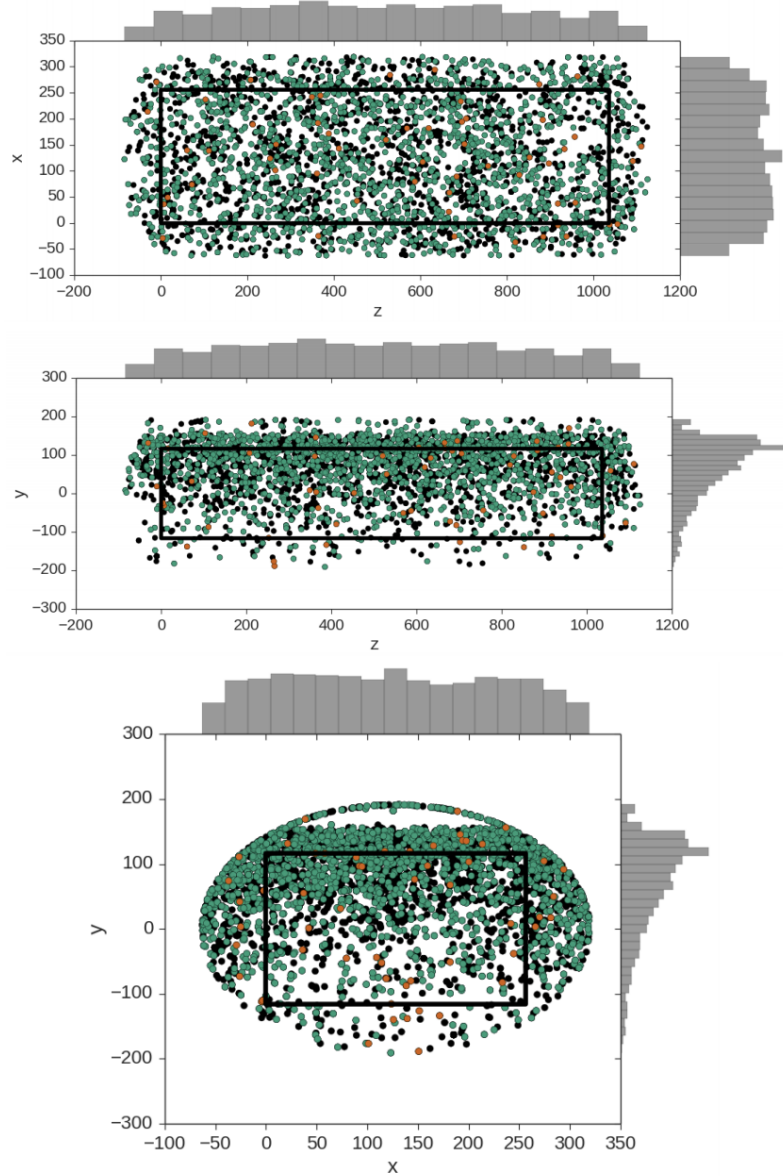


Figure 6.10: These plots show the decay point of actual cosmic π^0 's throughout any time in the 4.8 ms window. The green points represent neutron induced π^0 's, the orange represent photon induced π^0 's, and the black represent a π^0 that was produced from a charged particle. In each plot the black box is to represent the entire TPC dimensions not including fiducial cuts. Note that this is a stacked scatter plot with ordering; charged particle(black), photon(orange), neutron(green)

⁸⁸³ **Chapter 7**

⁸⁸⁴ **Results**

⁸⁸⁵ **Chapter 8**

⁸⁸⁶ **Conclusions**

Part I

887

Appendices

888